Growth process of *c*BN films from vapor phase

（和訳　気相からの *c*BN 薄膜の成長過程）

高村由起子

Growth process of *c*BN films from vapor phase

（和訳　気相からの *c*BN 薄膜の成長過程）

高村　由起子

Contents

1. Introduction

1.1. Why cubic boron nitride ?

Cubic boron nitride (*c*BN) is the zincblende-structured boron nitride which has "diamondlike" properties summarized in Table 1-1-1[1,2,3,4,5,6]. Its hardness, bulk moduli and theoritical thermal conductivity at room temperature are only second to diamond. The chemical stability against ferrous material[7] and thermal-chemical stability in presence of oxygen[5] are even superior to diamond, which make *c*BN an ideal material for application in machining of steels. High hardness, chemical- and thermal- stability, and high thermal conductivity of *c*BN generated interest of using this material for wear and corrosion resistant, which can be used in high temperature and/or corrosive environments. *c*BN also has high potential in applications as electronic devices and optoelectronic devices. *c*BN has a band-gap larger than diamond, which is suitable for blue to ultraviolet optical devices. And while diamond semiconductor is only successful in *p* type, *c*BN can be easily doped to be *p* and *n* type by doping Be as acceptors, and Si, S, KCN as donors, respectively[8]. Due to its large band gap, thermal stability and high thermal conductivity, it has a high potential for semiconductor working at high temperature as demonstrated by Mishima *et al.*[9], who fabricated *p-n* junction diode by *c*BN crystal which was functional at 650 ℃.

1.2. Polymorphism and phase diagram of BN

Boron nitride, analogous to carbon, has four crystalline allotropes, i. e. two sp^2 hybridized phases, hexagonal BN (*h*BN), rhombohedral BN (*r*BN), and two sp^3 hybridized phases, wurtzite BN (*w*BN) and cubic (zinc-blende) BN. There are also two more allotropes

Table 1-1-1 The selected properties of cubic boron nitride

lattice parameter (A)	3.615	
mass density (g/cm^3)	3.5	
hardness (GPa)	29.89-43.12 (Knoop hardness , single crystal)	[1]
	49-54 (Vickers hardness , polycrystalline)	[2]
bulk moduli (GPa)	369	[3]
thermal conductivity (W/cmK)	13 (at room temperature, theoritical)	[4]
thermal stability	no change in vacuum, slowly oxidized in air, when heated to over 2273 K	[5]
chemical stability	unaffected by usual acids	[5]
band gap (eV)	> 6 (indirect)	[6]

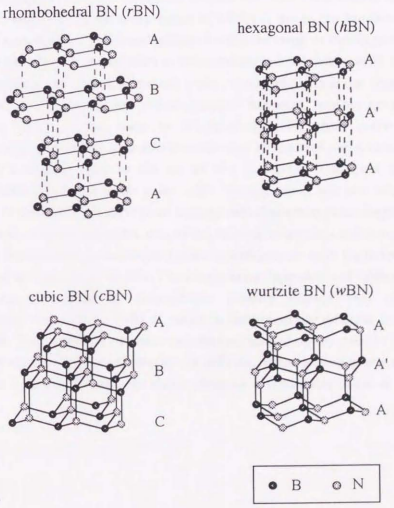

Figure 1-2-1 Structures of polymorphs of boron nitride

with random structure, turbostratic BN (*t*BN) [10] and amorphous BN (*a*BN) which are sp^2-hybridized phases. Graphitic (sp^2-bonded) *h*BN, *r*BN, and *t*BN consist of BN atomic layers, but differ in their stacking sequences which are shown in Figure 1-2-1. *h*BN has twofold stacking (AA'AA'), whereas *r*BN has threefold stacking (ABCABC). In *t*BN, BN atomic layers are stacked roughly parallel to each other but show random rotation and translation about the layer normal, and the distance between the layers (0.35 nm) is slightly larger than the value 0.33 nm for *h*BN[10]. *w*BN and *c*BN are analogous to hexagonal diamond[11] and cubic diamond, respectively, and their stacking sequences of major planes resembles *h*BN and *r*BN, respectively.

Figure 1-2-2 (a) shows a generally accepted P-T phase and reaction diagram cited from Ref. 12. The diagram was constructed using the results of shock-compressions and static high-temperature high-pressure systems in pressure range of 4-13 GPa, in addition to a diagram constructed by Bundy *et al.*[13]. In the range of the diagram, *h*BN, *c*BN and liquid were the thermodynamically stable phases, and in analogy with the phase diagram of carbon, *h*BN was predicted to be a thermodynamically stable phase at standard pressure and temperature conditions. *w*BN forms from static compression of *h*BN at much lower temperature compared to *c*BN[13], and also from shock compression of *h*BN[14] due to the similarity in stacking sequence. *w*BN was considerd to be a metastable phase in the range of the diagram because *c*BN with a catalyst did not convert to *w*BN at temperature just below the *w*BN-to-*c*BN direct conversion condition, and the *w*BN formation was considered to occur just because it was the only option the atoms had for the rearrangements. Recently, another proposal for P-T diagram (Figure 1-2-2 (b)) was made by Solozhenko[15,16], which predicts *c*BN as a thermodynamically stable phase at standard conditions. He pointed out several problems of Corrigan-Bundy's diagram, such as the use of the "catalytic" transition data, and the evaluation of *h*BN-*c*BN-liquid triple point, *c*BN melting curve and low temperature-low pressure region of the *h*BN-*c*BN curve from analogy with the carbon phase diagram. He carried out measurements on thermodynamic properties, thermal expansion and compressibility of four crystalline forms of BN, and calculated phase equilibrium curves in the temperature range of 0-4000 K and pressure up to 10 GPa. The temperature dependence of Gibbs energy for BN polymorphic transformation at atmospheric pressure showed that *c*BN remains thermodynamically stable up to 1570 K, which is fundamentally different from Corrigan-Bundy's diagram. The results of *ab initio* calculations carried out by Albe[17] support this proposal. Since experimental confirmation is difficult, there is continuous discussion on whether *c*BN is a thermodynamically stable phase or a metastable phase at the standard condition.

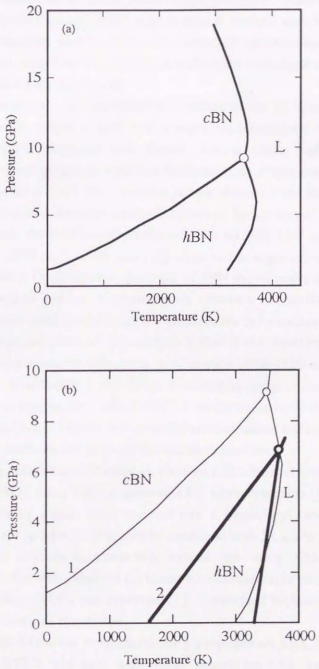

Figure 1-2-2 Proposed P-T diagrams of BN. (a) diagram constructed by Bundy *et al.*[13] and Corrigan *et al.*[12]. (b) diagram constructed by Solozhenko *et al.*[15]; 1 : curves from Bundy-Corrigan diagram, 2 : curves calculated by Solozhenko.

1.3. Characterization of the BN films

Phase identification of BN films needs careful attention. Generally, bonding analysis such as infrared (IR) spectroscopy, long range structural analysis such as electron diffraction, and compositional analysis such as X-ray photoelectron spectroscopy (XPS) are at least required for the phase identification of *c*BN. Identification with single analysis often leads to misidentification and misleading results.

The most commonly used identification method is the IR spectroscopy. Gielisse *et al.*[18] measured the IR reflection spectra of composites (compacts) of *c*BN single crystals synthesized from *h*BN, catalyzed with lithium nitride, under high pressure and high temperature. Analysis of spectra derived that Brillouin zone center transverse-optical (TO) mode frequency of *c*BN is 1065 cm^{-1}, and the sample showed a reststrahlen band near that region. Fahy[19] calculated the zone-center TO phonon frequencies of *c*BN using an *ab initio* pseudopotential linear-combination-of-atomic-orbitals method. The calculated value for the unstrained *c*BN was 1063 cm^{-1}, which was very close to the experimental value obtained by Gielisse *et al.*[18]. Since IR absorption spectrum of *h*BN shows peaks around 1370 cm^{-1} and 783 cm^{-1} due to in-plane and out-of-plane lattice vibration respectively[20], existence of cubic phase can be easily distinguished, and the quantitative information can be obtained as IR absorbance. The dangerous point of this analysis is that if the substrate is silicon, there is a possibility of misinterpreting the absorption peak around 1070-1100 cm^{-1} associated with O vibrational modes in Si network[21] as *c*BN peak shifted by compressive stress or some other reasons. However, the absorption peak of *c*BN TO mode is relatively wide when compared to the narrow peak of Si-O-Si TO mode, so the careful measurements and combination with other phase identification methods will prevent the misidentification.

For long range order structural analysis, electron diffraction is commonly used instead of X-ray diffraction (XRD), since XRD is unsuitable for nanocrystalline thin film like BN film synthesized from vapor phase. This method has a possibility (and actual reports) of misinterpreting copper as *c*BN, so it should be combined with IR analysis.

Compositional analysis is commonly carried out using XPS or Auger electron spectroscopy (AES). Recently, analysis on boron-to-nitrogen ratio with high precision using neutron depth profiling (NDP) was reported[22]. Rutherford backscattering spectroscopy (RBS) is also used in some of the studies.

Other phase identification methods recently proposed are AES, XPS, electron energy loss spectroscopy (EELS) and near edge X-ray absorption fine structure spectroscopy (NEXAFS). AES can be used as a phase identification method at the film surface by comparing the fine structure of Auger spectra of the samples to the spectra ("fingerprints") obtained from standard samples[23]. However, this method provides only qualitative information, and due to surface sensitivity of the method, careful attention to surface contaminant effect on the spectra is necessary. XPS spectra can be used for detection of sp^2-bonded phase by observing the π plasmon loss feature[23] which appears near the core-level peaks. EELS[24]

and NEXAFS[25,26] spectra can be used for phase identification by their π^* feature and comparing fine structure to the standard spectra. In both methods, a spectrum is obtained from the absorption process of atoms, so it provides highly localized information which is unaffected by the crystal size or the crystallinity of the sample. EELS has an advantage of obtaining information from local area as small as 1 nm^2, when it is combined with a field emission transmission electron microscope (FETEM). NEXAFS has an advantage of obtaining informations on nitrogen voids and interstitials[27,28]. These characterization methods will be especially useful for the study of micro- and nano-structure of the BN films.

1.4. Review on synthesizing methods of *c*BN

Since Wentorf[5,8] succeeded in synthesizing *c*BN by applying high temperature and high pressure to *h*BN with some catalysts, methods for synthesizing *c*BN for commercial use has not been drastically changed, and it is still the High Temperature - High Pressure (HTHP), solid-to-solid, method which is widely used. However, the produced *c*BN crystals have limitation in size and shape, and their applications are limited to abrasive grains or sintered tools. For applications in the fields of hard coatings, optics or electronic devices, synthesizing *c*BN in film form, on the substrate, at low temperature and in good crystallinity are desirable. The vapor deposition process of *c*BN has been thus studied and developed.

1.4.1. High pressure methods

*c*BN was first synthesized by HTHP method in analogy with diamond synthesis from graphitic material. Wentorf [5,8] applied high temperature (typically 2073 K) and high pressure (typically 8.6 GPa) to *h*BN with catalysts such as alkali and alkaline-earth metals, their nitrides, and antimony, tin and lead, which resulted in the first successful synthesis of *c*BN. Several years later, Bundy and Wentorf[13] reported direct (without catalyst) transformation of *h*BN to *c*BN at high temperature (2000 K) and high pressure (11.5 GPa) resulting in a crystallite size of about a micron or less. They reported that at high temperatures (2500-4000 K), the cubic form was favored, and at low temperatures (300 K), the wurtzite form was favored.

*c*BN can be synthesized at temperature as low as room temperature with shock compression (dynamic pressure) or high static pressure, if the starting material is chosen properly. Sato *et al.*[29] succeeded in formation of *c*BN from *r*BN by explosive shock compression(40-100 GPa), while the compression of *h*BN in the same condition resulted in formation of *w*BN. Ueno *et al.*[30] carried out static pressurization (~55 GPa) of *r*BN at room temperature with *in situ* X-ray diffraction. The result was successful, and they confirmed that direct transition from *r*BN to *c*BN starts at pressure of 8 GPa. In both cases, the direct diffusionless transition of *r*BN into *c*BN, expected by the similarity of stacking sequence

between *r*BN and *c*BN (see Fig. 1-2-1), was considered as the formation mechanism.

The largest *c*BN crystal was synthesized using the temperature difference method developed by Mishima *et al.*[31]. At pressure of ~5.5 GPa and temperature of ~2073 K, using $LiCaBN_2$ as a solvent, they succeeded in synthesizing a *c*BN crystal in size as large as 3 mm.

1.4.2. Low pressure methods

For the successful low pressure vapor deposition of *c*BN film, the kinetic energy transport to the growing surface is required, and in most cases the energy is transported by accelerated ions. The methods can be devided into two groups, the ion beam methods and plasma assisted methods.

Ion beam methods have an advantage of quantitative control of ion energy and ion flux, which is important in studying the growth environment of *c*BN. Ion beam methods can be further devided into two growps, the direct ion beam deposition methods and the ion beam assisted methods.

The direct ion beam methods have been attempted at the very early stage of development of low pressure *c*BN synthesis[32,33]. As one of the possibilities of film deposition from high energy and high momentum, Weissmantel *et al.* proposed the synthesis of metastable phase, and demonstrated the boron nitride film deposition[32,33]. As a result of molecular ion beam deposition using borazine ($B_3N_3H_6$), they obtained BN films with high hardness, and confirmed the existence of fine crystalline *c*BN by electron beam diffraction. After their work, several attempts has been reported[34,35], but gradually researchers shifted to ion beam assisted deposition. Recently, mass separated ion beam deposition (MSIBD) technique was applied to boron nitride film synthesis by Hofsaess *et al.*[36]. They succeeded in depositing *c*BN film on silicon substrate directly from purely $^{11}B^+$ and $^{14}N^+$ ions with well-determined energy and flux. The ion energy required for the *c*BN formation was 125 eV.

In the ion beam assisted methods, nitrogen and rare gas (commonly argon) ion beams are combined with boron source such as electron beam evaporated boron, laser ablated boron/boron nitride or sputtered boron/boron nitride. Kester *et al.*[37] used ion beam-assisted evaporation of boron for the preparation of *c*BN film. The apparatus consisted of two ion guns, one for nitrogen and one for rare gas. Boron was evaporated by electron beam evaporator. The optimum ion energy for the formation of *c*BN using nitrogen and argon was 500 eV. They also succeeded in synthesizing *c*BN films using other combinations of gases, such as, nitrogen and krypton, nitrogen and xenon, and only nitrogen. By studying effect of the mass, the energy and the flux of ions on *c*BN concentration of the deposited film, they found that the *c*BN formation is momentum-induced rather than energy-induced. Friedmann *et al.*[38] used ion-assisted pulsed laser deposition (IAPLD) for the *c*BN film deposition. Laser ablation of *h*BN target was assisted by nitrogen and argon ion source. They found that the films containing high percentage of *c*BN were deposited with ion/atom arrival values of near unity at ion energy between 800-1200 eV.

Compared to the ion beam methods, plasma assisted methods have possibilities in high deposition rate, large area deposition and low cost apparatus, which are required for a commercial method. In order to successfully synthesize *c*BN, ions have to be accelerated to certain energy before reaching the growing surface of the film. In most cases, RF power is applied to the substrate, and ions are accelerated across the potential difference between the plasma and the substrate RF bias voltage. The ion energy dependence of *c*BN formation in plasma assisted methods is nearly always discussed using the substrate bias voltage which is not exactly the energy of the accelerated ions. Mieno *et al.*[39,40] succeeded in synthesis of *c*BN film using RF bias sputtering of a *h*BN target. The optimum negative substrate bias voltage for the *c*BN formation was 400 V. McKenzie *et al.* used reactive ion plating for the *c*BN film deposition. Boron was evaporated from an electron beam source through magnetically confined and intensified argon and nitrogen plasma[41], later a helicon plasma [42], and substrate was RF biased for the ion energy control. Kidner *et al.*[43] carried out BN film deposition by RF sputtering of a hot pressed *h*BN target, and used an electron cyclotron resonance (ECR) ion source as high density ion source and negative substrate bias voltage for substrate bombardment. They succeeded in obtaining *c*BN films with negative substrate bias voltage as low as 105 V, probably due to high ion flux from ECR ion source.

*c*BN films can be also successively deposited from gas source. Ichiki *et al.*[44] prepared *c*BN films by low pressure inductively coupled plasma enhanced chemical vapor deposition (ICP-CVD) with B_2H_6+N_2+He+Ar gas system. RF power was applied to the substrate, and the optimum potential difference between plasma potential and substrate bias potential for the *c*BN formation was reported as 80-86 V, which is relatively small compared to the optimum energy reported in physical vapor deposition methods. This low energy threshold is mainly attributed to the high ion flux from the high density plasma.

1.5. Optimum growth environment and proposed formation and growth mechanisms of *c*BN

Ion energy (or momentum), stoichiometry and substrate temperature must be optimized for the successful growth of a *c*BN film. The threshold energy, which is a minimum energy required for *c*BN formation, varies from about 100 eV to 1000eV, depending on process and other experimental conditions. Boron-to-nitrogen ratio of *c*BN containing films reported in many papers were near stoichiometry, and since *c*BN has not been found in off-stoichiometric films, stoichiometry is considered to be one of the important factors to stabilize *c*BN[22,45]. Substrate temperature is also an important factor for *c*BN formation. Kester *et al.*[46] reported that a minimum substrate temperature of 200-300℃ is required for the deposition of high *c*BN containing film. Friedmann *et al.*[38] reported that the optimal substrate temperature window in IAPLD of *c*BN film is 150℃ to 500℃. Hofsaess *et al.*[47] reported the substrate temperature threshold of 150℃ for *c*BN formation in MSIBD. The reason for

the existence of low temperature threshold is not clear.

Typically, ion beam assisted methods require relatively higher ion energy, while the threshold energy is lower for plasma assisted methods. Among plasma assisted methods there is a trend that the higher the plasma density is, the lower the threshold energy, which may be a result of trade off between flux and energy. Kester *et al.*[37] clarified this point by revealing that *c*BN formation scales with momentum-per-deposited boron by studying the gas species and flux dependence of *c*BN formation in ion beam assisted evaporation of boron. Mirkarimi *et al.*[48] also observed similar momentum-like ($(M_{ion}E_{ion})^{1/2}$) scaling of *c*BN formation in IAPLD. Film properties which show the similar scaling on ion energy is the density and the compressive stress generated by atomic peening[49,50]. These experimental results strengthen, but do not guarantee, the compressive stress-induced model and the subplantation model, which are now the two major models of the formation mechanism of *c*BN.

The compressive stress-induced formation of *c*BN was primarily proposed by McKenzie *et al.*[41], in the light of high compressive stress, typically 5 GPa or in some case 10-25 GPa[51], generated in *c*BN films. Their model suggests that the ion irradiation induces a "thermal spike" which locally melts the growing surface of the BN film, and with the hydrostatic component of biaxial compressive film stress, the material solidifies under high temperature-high pressure condition wherein *c*BN is thermodynamically stable. Based upon his experimental results, he suggested that threshold compressive stress value is about 3 to 4 GPa. But this model cannot explain the low temperature threshold of *c*BN formation, because according to their idea of "thermal spike", local groups of atoms should be in much higher temperature condition compared to the substrate temperature, aside from adequacy of the definition of temperature with small numbers of atoms.

On the other hand, subplantation model was primarily proposed by Lifshitz *et al.*[52,53] for the film growth from hyperthermal species (1-1000 eV). The model would be described by energetic particle penetration into subsurface layer, stopping of the particle and dissipation of energy by means of atomic displacements, phonon excitations and electron excitations, and subsequent subsurface growth. This model was applied to the growth of tetrahedral amorphous carbon[54], and it is believed that the local densification leads to the formation of denser phases. This model also cannot explain the low temperature threshold of *c*BN formation.

Both models are correlated in terms of forced densification, because forced densification causes compressive stress. These models partly succeeded in explanation of the growth of amorphous diamond like carbon films. But since there are many differences between *c*BN and amorphous carbon films, such as crystallization in *c*BN and opposite trend in substrate temperature dependence, which seem to be related to the ionicity of BN bonds, the models cannot be easily applied to *c*BN formation mechanism[55]. And so far, these models has failed to explain the peculiar layered structure of *c*BN films observed in a cross-sectional high resolution transmission electron microscope image obtained by Kester *et al.*[56]. The image revealed the existence of sp^2-bonded layer as an initial layer between the substrate and the *c*BN layer. The initial layer consisted of amorphous layer and *t*BN layer which was oriented with its

c-axis parallel to the substrate surface. This initial layer has formed under the same deposition condition which *c*BN formation occured, so even if the vapor condition is controlled properly, *c*BN will not form until the surface condition is satisfied for *c*BN formation. After Kester *et al.*'s work[46,56], several groups made cross-sectional TEM observation of *c*BN films deposited in various deposition processes[57,58,59,60,61]. So far, similar structure has been observed in these studies, and it is considered that the initial layer formation prior to the *c*BN formation is common process in vapor deposition of *c*BN films. But the exact role and condition of this initial layer in *c*BN formation is not well understood. Interesting point is that the thickness of this layer varies depending on deposition process and condition. This means that the initial layer satisfies the *c*BN formation condition after growing to thickness of a few to 100 nm which depends on vapor condition. Thus revealing the change during the initial layer growth will be important for the study on *c*BN formation mechanism, but owing to its experimental difficulty, the study on initial layer evolution has not yet been carried out successfully.

1.6. Why not *c*BN ? — the purpose of this study

The biggest problem prohibiting the commercial use of *c*BN films is the delamination from the substrates. The causes for this problem are considered to be the high compressive film stress in the film, and the poor adhesion of the film to the substrate. Since stress inside the film builds up with the increase in thickness, the thickness of the film without peeling off from the substrate is limited to a few hundred nm for most cases, which is insufficient for hard coating of machining tools. Even if the thick film is obtained, it will start to delaminate as soon as, or maybe an year after, it is taken out from the chamber. This is considered to be the effect of the moisture in the air. The instability of the *h*BN film exposed to the moisture has been reported in several papers. Matsuda *et al.*[62] reported that when the transparent *h*BN film (they call it a plate, and it seems to be *t*BN) was exposed to the air, it became gradually cloudy, gained weight and finally cracks with NH_3 odour. Considering these effects, it seems that initial *t*BN layer is the main cause of instability under the existence of moisture in case of *c*BN film. The existence of the thick initial layer itself is another problem, because when a very thin *c*BN film of about 10 nm was required for tribological coating, the film would not contain *c*BN because of insufficient thickness of initial layer. Another large problem is that the synthesized *c*BN films are polycrystalline and its typical crystal size is around 20-40 nm. Intending the application of *c*BN film in high-power high-temperature electronic device, this problem should be solved, and epitaxial growth of single crystal *c*BN film is desirable.

In solving above problems, initial layer holds the key. Study on the origin and the evolution of this layer and investigating a role of initial layer in the formation process of *c*BN is necessary, and it will be connected to the control and the reduction of this layer. This kind of initial layer is also observed in other metastable films grown in ion assisted vapor

deposition[63], so the results of study on this initial layer have possibility of revealing the formation mechanism of other metastable phase under energetic ion bombardment, and ultimately the hetero-epitaxial growth of these materials for the application as electronic devices.

2. Bias sputter deposition of *c*BN films

2.1. Bias sputtering apparatus

In this study, phase-regulated unbalanced-magnetron RF bias sputtering apparatus was used for the film synthesis, and its schematic diagram is shown in Figure 2-1-1. Its main part consists of a 30 liter cylindrical chamber made of stainless steel, turbomolecular pump and oil rotary pump, two electrodes, two matching boxes, two RF power amplifiers and a phase controller. RF power (frequency : 13.56 MHz) was applied to both target- and substrate-electrodes by two different amplifiers so that the energy of target- and substrate- impinging ions can be controlled independently by different bias voltages applied to the two electrodes. In order to reduce dephasing, and to obtain a stable plasma, RF signals sent to the two amplifiers were synchronized by the phase controller, and their phase difference was controlled[64]. The phase regulation also changed the ion energy distribution[65] whose effect on *c*BN formation is not yet well understood. A ring-shape eternal magnet to form unbalanced "open" magnetic field was set inside the target electrode in order to confine the plasma, and increase the plasma density and the flux of substrate impinging ion. Quadrupole mass spectrometer (QMS) and ion energy analyzer (IEA) were equipped inside the substrate electrode, and its ground was RF driven with the electrode in order to obtain quantitative informations such as energy, mass and flux of substrate impinging species accelerated across the potential difference between plasma and substrate electrode.

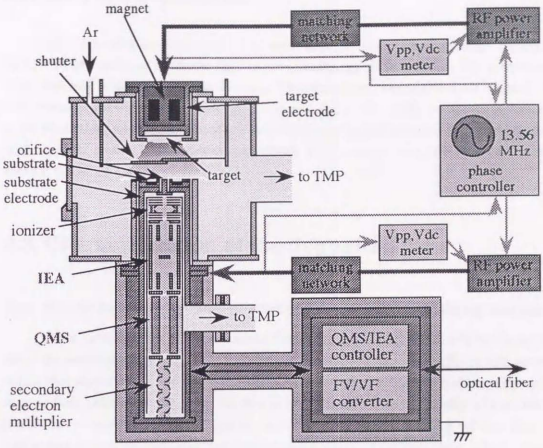

Figure 2-1-1 Schematic diagram of phase-regulated unbalanced-magnetron RF bias sputtering apparatus

Table 2-2-1 Experimental conditions

rf power input (target)	600W～2000W
substrate bias voltage	-50～-400V
(rf power input (substrate))	50W～500W)
phase angle difference	0°
working pressure	5～40mTorr
sputtering gas	Ar
gas flow rate	40sccm
distance between the electrodes	40mm
target	sintered *h*BN disk
substrate	Si(100) 32mm×32mm, t=0.2, 0.6mm
magnetic field	150G
	(at the center of the substrate electrode)

2.2. *c*BN film deposition

*c*BN films were deposited on 32×32 mm^2 sized, *p*-type, 〈100〉 oriented silicon wafer by RF bias sputtering of a sintered *h*BN target (KD-3S, ShinEtsu Kagaku). For sputtering gas, argon was used with no additional nitrogen. The depositions were carried out without QMS-IEA measurements. Typical deposition conditions used in this study are shown in Table 2-2-1. All depositions were carried out after presputtering target and substrate for 15 to 30 minutes, with a pair of shutter between electrodes closed. A photogragh of a *c*BN film coated silicon wafer is shown in Figure 2-2-1.

2.3. Characterization of the deposited films

2.3.1. Fourier transform infrared spectroscopy - Vibrational bonding analysis

Phase identification of the deposited films were mainly accomplished by transmission micro Fourier Transform InfraRed (FTIR) spectrometer (FT/IR-700, JASCO). Measurements with a spot size of 200×200 μm^2 were carried out through the films with silicon substrates, as soon as they were taken out from the deposition chamber. The uniformity of the films was studied by measuring spectra at regular intervals of 3 mm from edge of the film. The background spectra was obtained from the near edge region of each specimen where films were not deposited because of the substrate cover.

Fig.2-3-1-1 shows a typical IR spectra of a *c*BN film successfully synthesized by this method, showing a peak associated with *c*BN at 1080 cm^{-1}. The shift of *c*BN peak to higher wavenumbers from the literature value has been frequently reported in measured IR spectra of *c*BN films[38][41], and it is a result of the strained-state of crystallites[19] due to high compressive stress in the deposited film. There are two peaks associated with *h*BN, which indicates that this film is not a single-phase film. FTIR measurements with 3 mm intervals across the films revealed that the films are uniform in formed phases and thickness for at least in the area of 24×24mm^2 at center of the substrates. The ununiformity at the edge of the film is considered to be a shadowing effect of the substrate cover. So by making window of the substrate cover larger, the uniform films are expected to be deposited in larger area. Large area deposition of uniform *c*BN film is possible unless uniform plasma is sustained by large area electrodes.

2.3.2. Transmission electron diffraction - Structural analysis

Transmissiom electron diffraction (TED) inside the transmission electron microscope was used for long-range order structural analysis, since the size of *c*BN crystallites, which is about 20 to 40 nm, is not suitable for the X-ray diffraction measurement. Fig. 2-3-2-1 is a

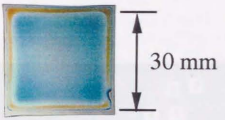

Figure 2-2-1 A photograph of *c*BN film coated Si (100) wafer

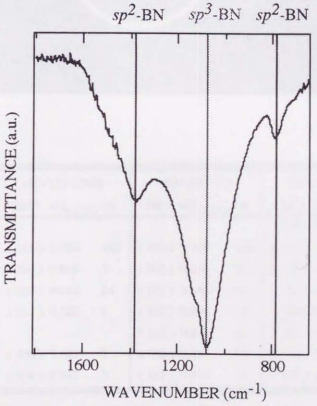

Figure 2-3-1-1 A transmission FTIR spectrum of a *c*BN film, indicating strong absorption at 1080 cm^{-1}.

typical TED pattern of a *c*BN film obtained by 200 kVTEM. The ring pattern shows that the deposited film is polycrystalline and randomly oriented. The ring diameters compared to the interplanar spaces and relative intensities of powder diffraction data[66] of *c*BN(identification number 35-1365), *w*BN(26-773) and *h*BN(34-421) showed that the film contains *c*BN (not *w*BN) and *t*BN (or *h*BN, *r*BN with low crystallinity).

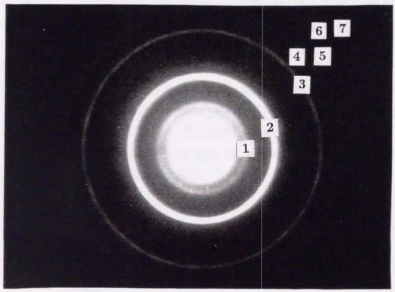

Observed value			*c*BN (35-1365)		*w*BN (26-773)		*h*BN (34-421)	
No.	d/d_2	Int	(hkl)	$d/d_{c(111)}$ Int	(hkl)	$d/d_{w(100)}$ Int	(hkl)	$d/d_{c(111)}$ Int
1	1.583	S					(002) 1.594	100
2	1.000	VS	(111) 1.000	100	(100) 1.000	100	(100) 1.039	15
			(200) 0.866	5	(002) 0.956	70	(101) 0.988	6
3	0.613	M	(220) 0.612	24	(101) 0.886	45	(102) 0.870	9
4	0.526	W	(311) 0.522	8	(102) 0.691	18	(004) 0.797	6
5	0.503	W			(110) 0.578	25	(103) 0.743	<1
6	0.433	VW	(400) 0.433	2	(103) 0.537	16	(104) 0.632	2
7	0.397	VW	(331) 0.397	3	(112) 0.494	12	(110) 0.600	5

Figure 2-3-2-1 A transmission electron diffraction pattern of a *c*BN film. Interplanar spaces and relative intensities were cited from Ref. 66.

2.3.3. X-ray photoelectron spectroscopy - Compositional analysis

Composition and chemical state of the deposited film surface were examined by an X-ray photoelectron spectrometer (XPS-7000, Rigaku Denki) with an X-ray source of nonmonochromatized Mg K_α radiation (1253.6 eV). The analyzer was operated at 15 eV pass energy providing 1.2 eV resolution. Binding energy was calibrated by C1s line at 284.6 eV[67]. Depth profile was obtained by ion milling by argon ion beam with energy of 500 eV, and ion current of 0.1 mA. No surface treatment of the film was done before these measurements.

Figure 2-3-3-1 shows a wide XPS spectrum of a *c*BN film. Nitrogen-to-boron ratio was near stoichiometry, and beside boron and nitrogen, it contained about 1at.% of argon. Carbon and oxygen were also detected. Figure 2-3-3-2 shows the etched depth dependent XPS spectra for boron, nitrogen, silicon, and oxygen. Carbon has been sputtered away with the first ion beam etching process, which indicates carbon observed in Fig. 2-3-3-1 is a surface contaminant. Oxygen, on the other hand, existed throughout the film, but it was unclear whether oxygen was incorporated in the film during the deposition or after it was exposed to the air. Nitrogen found in silicon substrate is considered to be the result of nitrogen ion bombardment during the presputtering process. The origin of nitrogen in sputtering gas is recombined of nitrogen atoms which are sputtered from the target.

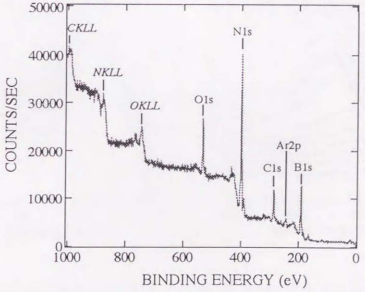

Figure 2-3-3-1 A wide XPS spectrum of *c*BN film surface. Core level peaks from B 1s, N 1s, C 1s, O 1s, Ar 2p and Auger peaks from O, N, C are apparent.

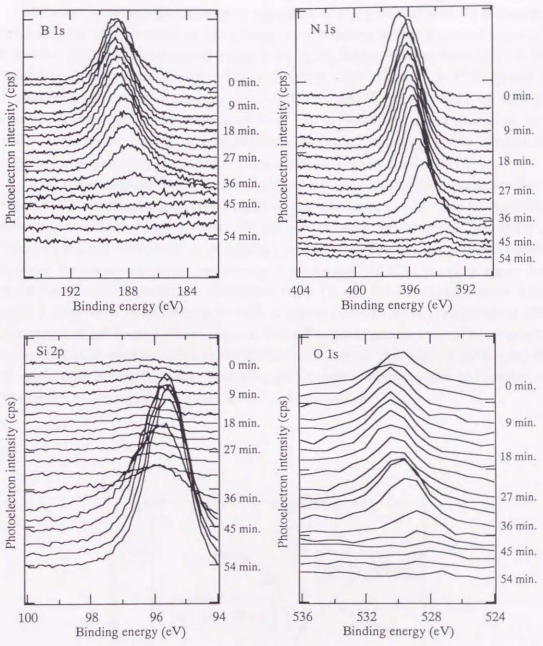

Figure 2-3-3-2 Depth profile of B 1s, N 1s, Si 2p and O 1s XPS spectra. Each measurement were carried out after 3 minutes ion beam sputtering of 500 eV Ar^+ ion beam, except for the first measurement.

2.4. Optimization of the deposition condition

The most contributing experimental parameter to the *c*BN formation in bias sputter deposition is the negative substrate bias voltage, since it determines the energy of ions which bombard the growing film surface[40]. Figure 2-4-1 shows the bias voltage dependence of *c*BN formation using IR absorbance obtained from 1080 cm^{-1} and 1380 cm^{-1} in FTIR spectra of each sample. Under negative substrate bias voltage of 200 V, the formation of *c*BN (IR absorbance at 1080 cm^{-1}) was not observed. Over 250 V, *c*BN films were deposited but they contained certain amount of sp^2-bonded BN phase. Negative bias voltage of 300 Vseems to be the optimal condition since the deposited film contained highest amount of *c*BN.

Dependence of phase formation on target power and sputtering gas pressure are shown in Figure 2-4-2 and Figure 2-4-3. *c*BN formation was confirmed in wide range of deposition conditions, and constant IR absorbance for sp^2-bonded phase was observed. The origin of sp^2-bonded BN phase was revealed by measuring the deposition time dependent IR absorbances. The results for negative substrate bias voltage of 250 V and 300 Vare shown in Figure 2-4-4. Both figures show constant IR absorbance value for sp^2-bonded phase whereas linear increase is observed in IR absorbance for *c*BN. It means that *c*BN grows in single phase after certain amout of sp^2-bonded phase has grown. The difference in plateau value of IR absorbance between the two conditions indicates the difference in critical thickness of sp^2-bonded BN layer, where *c*BN formation occurs. Sputtering gas pressure and target power had small effect on the critical thickness of sp^2-bonded layer for this condition.

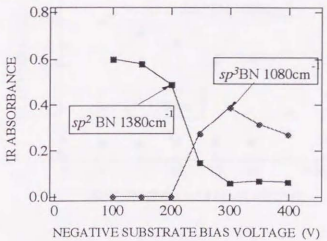

Figure 2-4-1 Substrate bias voltage vs IR absorbance of the deposited films. Target power : 2000W, Ar flow rate : 40sccm, Ar pressure : 20mTorr, deposition time : 2min, Si substrate thickness : 0.6mm.

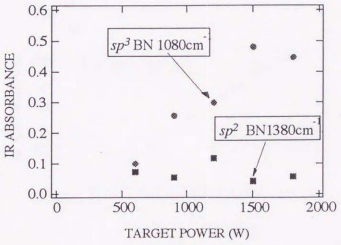

Figure 2-4-2 Target power vs IR absorbance of deposited films. Ar flow rate : 40sccm, Ar pressure : 20mTorr, substrate bias voltage : -300V, deposition time : 3 min.

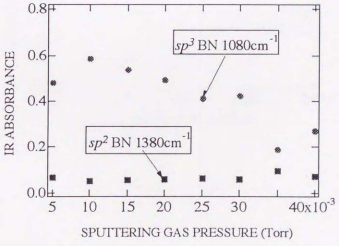

Figure 2-4-3 Sputtering gas pressure vs IR absorbance of deposited films. Ar flow rate : 10sccm, substrate bias voltage : -300V, deposition time : 3 min.

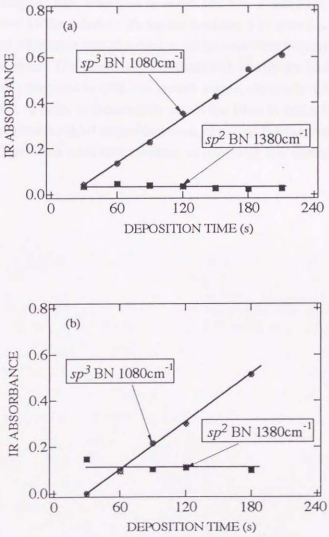

Figure 2-4-4 Deposition time evolution of IR absorbance, indicating the difference of initial layer thickness. (a) Target power : 2000W, substrate bias voltage : -300V, Si substrate thickness : 0.2mm. (b) Target power : 2000W, substrate bias voltage : -250V, Si substrate thickness : 0.6mm.

2.5. Conclusions

Uniform *c*BN films were successfully and stably synthesized in wide range of experimental conditions using phase-regulated unbalanced-magnetron RF bias sputtering apparatus. By suppressing the film thickness to under 200 nm, it was possible to obtain *c*BN films which stays adhered to the substrate during the analyses. The growth of sp^2-bonded layer preceding the growth of *c*BN layer was observed in deposition time dependent IR absorbance of *c*BN and sp^2-bonded phase. The purpose of this study is to clarify the formation and growth mechanisms of *c*BN, so *c*BN films in different growth stages, especially films in initial layer growth stages are needed. In order to successfully obtain the films in initial layer growth stage, which means films deposited for short deposition time, the films for the study in next chapter were prepared with a deposition condition resulting in relatively low deposition rate.

3. Analysis of *c*BN films in different growth stages

3.1. Film preparation for the study of growth process

The films were prepared by bias sputter deposition described in the previous chapter.The deposition conditions are shown in Table 3-1-1. The condition was maintained constant except for the deposition times ranging from 30 s to 300 s, in order to obtain *c*BN films in different growth stages. The thickness of the film deposited for 300 s were measured from cross-sectional scanning electron microscope (SEM) image, and it was about 110 nm. All the samples stayed adhered to the substrates without peeling off during the analysis.

Table 3-1-1 Deposition condition of specimens for study of *c*BN films in different growth stages

Deposition condition	
target power	600 W
substrate bias voltage	-300 V
(substrate power	270 W)
phase difference	0°
working pressure	2.1 Pa
sputtering gas	Ar
gas flow rate	40sccm
Presputtering condition	
target power	500 W
substrate power	100 W
(substrate bias voltage	-90 V)

3.2. Fourier transform infrared spectroscopy

Transmission micro FTIR spectrometer (FT/IR-700, JASCO) were used for the phase identification by IR measurements. Measurements with a spot size of $200 \times 200\ \mu m^2$ were carried out through the films with silicon substrates, as soon as they were taken out from the deposition chamber. The background spectra was obtained from the near edge region of each specimen where films were not deposited because of the sintered *h*BN cover. IR absorbance evaluated from the IR spectra obtained from the center of the film was used as the representating value for the specimen.

3.2.1. Phase evolution

IR spectra and IR absorbances of sp^3 bonded phase (around 1080 cm^{-1}) and sp^2 bonded phase (around 1380 cm^{-1}) evaluated from the spectra of the films deposited with different deposition times are shown in Figure 3-2-1-1 and Figure 3-2-1-2. It shows that in initial growth stage, sp^2 bonded phase grows until the critical thickness, and then cubic phase forms and grows in a single phase. The cubic phase appears to be formed at 75 s, which was confirmed by the IR spectra in Fig. 3-2-1-1; the peak around 1080 cm^{-1} was not so clear, but faint increase of absorbance is apparent. The thickness of the films deposited over 120 s were measurable from cross-sectional SEM images. Assuming the time-linear growth of cubic phase and extrapolating these measured thickness to 75 s, where cubic phase forms, initial layer thickness of 50 nm was estimated. Approximate deposition rate of the initial layer, 0.7 nm/s, seems to be considerably higher than the deposition rate of cubic phase, 0.3 nm/s.

3.3. X-ray photoelectron spectroscopy

Composition and bonding state of the deposited film surface were examined by an X-ray photoelectron spectrometer (XPS-7000, Rigaku Denki) with an X-ray source of nonmonochromatized Mg Ka radiation (1253.6 eV). The analyzer was operated at 15 eV pass energy providing 1.2 eV resolution. Binding energy was calibrated by C1s line at 284.6 eV. No surface treatment of the films was done before these measurements. Especially for the *c*BN film deposited for 300 s, the very thin surface layer was examined by angle resolved XPS by changing the take-off angle by sample tilt in order to increase the surface sensitivity.

3.3.1. Compositional evolution

XPS analysis revealed that nitrogen-to-boron atomic ratio of the films were nearly stoichiometric throughout the samples regardless of the deposition time (Figure 3-3-1-1). Beside boron and nitrogen peaks, argon, carbon and oxygen associated peaks were observed in

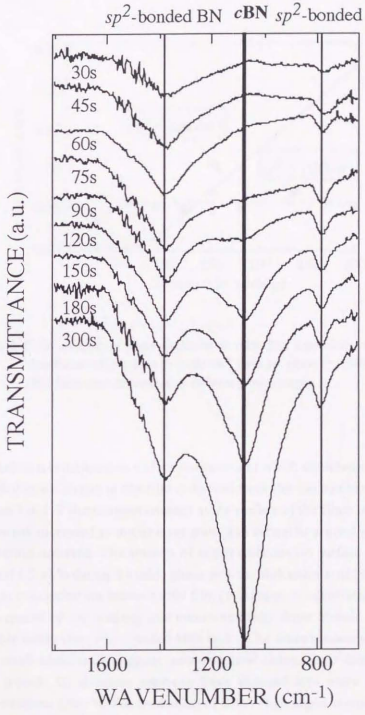

Figure 3-2-1-1 Transmission FTIR spectra of *c*BN films prepared with different deposition time. The films were prepared with a same deposition condition.

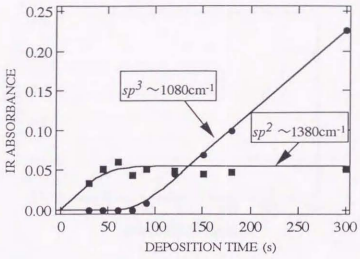

Figure 3-2-1-2 FTIR analysis of phase evolution in *c*BN film deposition process. IR absorbances of sp^3 phase (~1080 cm^{-1}) and sp^2 phase (~1380 cm^{-1}) in *c*BN films were determined in different growth stages.

every sample. Carbon is considered as surface contaminant which adsorbed on sample surface while it was handled in air. Argon in the film is derived from the ion bombardment during the film growth. Figure 3-3-1-2 shows argon content at the surface of the films in different growth stages. Argon content increased as initial layer grew, and saturated around where sp^3-bonded cubic phase formation occurred. The amount of argon embedded in surface seems to remain unchanged at about 1.5 at.% during the cubic phase growth. McKenzie *et al.*[41] have reported difference in argon concentration between *c*BN film (1 % argon concentration) and *h*BN film (undetectable) prepared by ion plating, and mentioned that dense atomic packing of *c*BN entraps argon more easily than the oriented *h*BN layer. The same tendency was observed in our case, and our result additionally suggests some structural change in sp^2-bonded phase during the initial layer growth. Its structure seems to have changed into more argon-trappable, pre-cubic, dense structure prior to the formation of *c*BN. High argon concentration in *c*BN phase compared to the initial layer is also reported by Ichiki *et al.*[68] who prepared *c*BN film by ICPCVD method, but the argon concentration was only 0.4 at.%. There was also a case in *c*BN film prepared by IAPLD which the difference in argon concentration between *c*BN phase and initial phase was not found[38]. Considering these various results, incorporation of argon is not a requirement for the *c*BN formation but a result of the formation of dense phase. Moreover, even if the dense phase has formed, the argon concentration depends on deposition

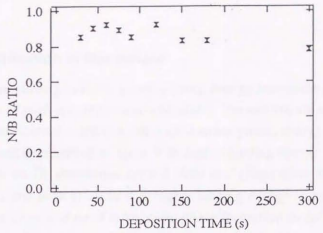

Figure 3-3-1-1 Nitrogen-to-boron ratio dependence on deposition time.

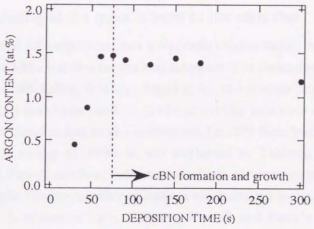

Figure 3-3-1-2 Argon content at the film surfaces of *c*BN films in different growth stages.

conditions, so there is a possibility of lowering argon concentration by choosing the deposition conditions properly. And since these films with different argon concentration were in equally highly compressive stressed state, argon incorporation itself is not a cause of internal film stress.

3.3.2. Phase identification of film surface

To identify the phase present in growing front, energy loss peaks from B1s core level peak in XPS spectra of each specimen were examined. The spectra are shown in Figure 3-3-2-1. If the film surface contains *h*BN or other sp^2-bonded phase, energy loss peak due to the π electrons[23] should be observed at about 9 eV higher binding energy from the core level peak. For films with no IR absorbance around 1080 cm^{-1} (deposition time t = 30∼60 s), additional π plasmon loss peak at about 9 eV higher binding energy from the core level peak was observed. For the films in state of initial cubic phase formation on sp^2 bonded layer (t = 75 ∼90 s) the peak was observed faintly. This result suggests that in this growth stage, sp^2-bonded phase and sp^3-bonded phase coexist at the growing surface. Coexistence of two phases are also reported by Barth *et al.*[69]and Ilias *et al.*[70]. The peak was not observed from the films containing high amount of cubic phase (t = 120∼300 s). Thus surfaces of these films are considered to be completely covered with *c*BN. Considering this result with the result of IR analysis, it seems that *c*BN nucleation condition was satisfied on local points over initial layer. And after the nucleation competitive growth with sp^2-bonded BN continued until *c*BN grains coalesce and cover the growing film surface.

3.3.3. The phase existing at the growth front of the *c*BN film

The angle resolved XPS was carried out with configuration shown in Figure 3-3-3-1. The *c*BN film deposited for 300 s was used for the measurement. The measurement was also applied to sp^2-bonded pyrolitic BN (pBN, ShinEtsu Kagaku) for the comparison. The samples were inclined to 70 degrees at maximum, and no evidence for the existence of sp^2-bonded phase which should arise in π plasmon loss peak was observed for *c*BN film. Inelastic mean free path of photoelectron with energy of 1000 eV was evaluated by Tanuma, Powell and Penn's formula[71]. Tanuma, Powell and Penn's formula evaluate electron inelastic mean free paths λ using molecular weight, density, number of valence electrons per molecule, bandgap energy, and electron energy. λ evaluated from Tanuma, Powell and Penn's formula using bulk properties of *c*BN and *h*BN were 2.1-2.2 nm and 1.6 nm respectively. The density and the band gap energy of the deposited film are considered to be different from the bulk value, but even if density of sp^2-bonded phase was as low as 1.5 g/cm^3, λ is still 2.0 nm. This result indicates that even if sp^2-bonded phase exists at the growing surface of *c*BN layer, its thickness should be considerably smaller than 0.7 nm.

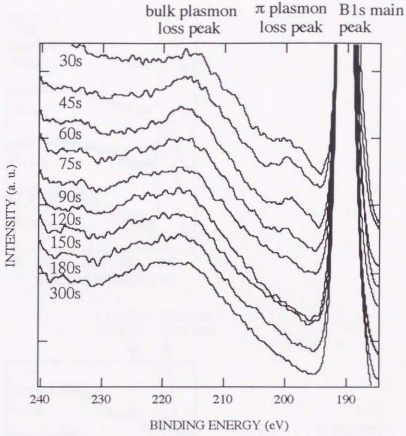

Figure 3-3-2-1 Phase identification of BN film surface by observing π plasmon loss features in XPS spectra.

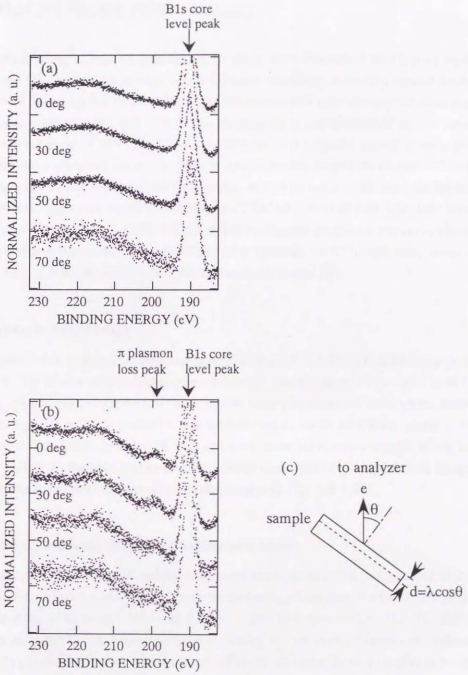

Figure 3-3-3-1 B 1s spectra obtained in angle resolved XPS analysis of (a) *c*BN film surface and (b) pBN. The spectra are normalized by setting the core-level peak intensity to unity. (c) shows the measurement configuration and the interrelations among inclining angle : θ, surface layer thickness contributing to the measurement : d, and electron inelastic mean free path : λ.

3.4. Atomic force microscopy

Surface morphology of the deposited films were examined by tapping mode AFM (Nanoscope III, Digital Instruments) under ambient condition. Humidity around the apparatus was about 40 % during the observations. In contrast with contact mode AFM, observed images were clear and reproducible due to its small imaging force and absence of lateral force. When the contact mode AFM was carried out on *c*BN films in different growth stages, the strong interaction were observed mainly in films in initial growth stages, which resulted in breaking AFM tips, and thus the distortion of the images. AFM tips made of silicon with tip radius of 5 to 10 nm and half cone angle of 18 degree (TTAFM, NANOSENSORS) were used. Drive frequency of the tip was about 300 kHz, and free oscillation amplitude was set to about 80 nm. Careful attention was paid to reproducibility of images observed through many scans and with different tips in order to avoid image distortion by damaged tips.

3.4.1. Surface morphology

Figure 3-4-1-1 shows tapping mode AFM images of *c*BN films in different growth stages. Figure 3-4-1-1 (a) is a surface image of an initial sp^2 bonded layer (deposition time t = 45 s). Likewise, (b) and (c) correspond to those of the films just after the cubic phase nucleated on the initial layer (t = 90 s) and after the surface was covered with cubic phase (t = 300 s) respectively. Grains of size about 20～40 nm were observed in every sample which is close to the size of *c*BN crystallites measured from transmission electron microscopic image. Figure 3-4-1-2 is the cross-sectional profiles of the images in Fig. 3-4-1-1.

3.4.2. Scaling analysis of morphological evolution

Quantitative analysis of surface roughness observed in AFM image could be done by a scaling analysis of root mean square (rms) roughness R_{rms}. Calculation of a scale dependent rms roughness using AFM height data was done by a method described in Ref. 72. Referring to Westra *et al.*'s work[73], when the average radius of the major features in observed AFM image is five times larger than the radius of AFM tip, decrease in rms roughness by distortion of the image is less than 2 %. The smallest average radius of an AFM image observed in this experiment was about 150 nm and the nominal tip radius was 5 to 10 nm. Since the AFM images of each samples were reproducible through many scans and with different tips, we considered that the tip damage was small enough so that decrease in calculated rms roughness by image distortion was less than 2 %.

Figure 3-4-2-1shows the scale dependent rms roughness of the films in Fig. 3-4-1-1 and Fig. 3-4-1-2. All curves are separated into two regions, which are scale-dependent part and

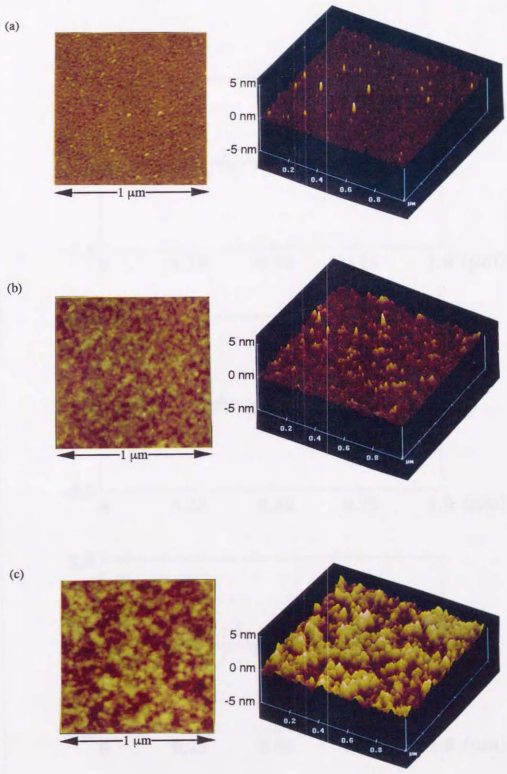

Figure 3-4-1-1 Tapping mode AFM images of *c*BN films in different growth stages. Deposition times: (a) 45 s, (b) 90 s, (c) 300 s.

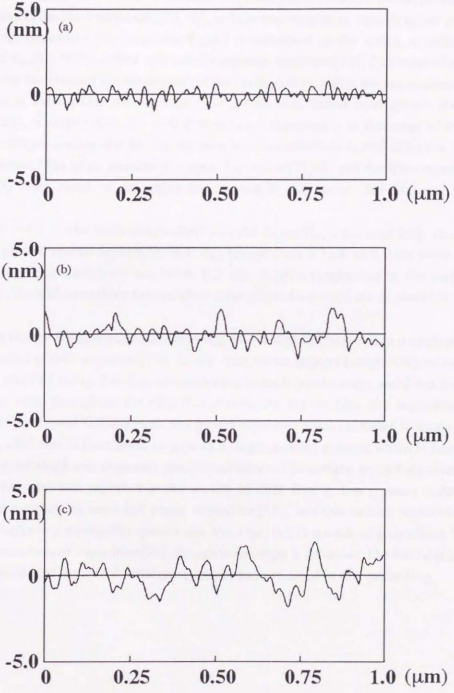

Figure 3-4-1-2 Cross-sectional profiles of the *c*BN film surface in different growth stages. Deposition time, (a) : 45s, (b) : 90 s, (c) : 300 s.

scale-independent part. The scale-independent rms roughness estimated from a large scale part of the curve in Fig. 3-4-2-1 would be "the rms roughness", which we can use as a representative value when we compare the surface roughness between different samples. It has recently been revealed that in some films when the scale is small enough, fractal nature of the surface roughness becomes noticeable[74,75], and the rms roughness depends on its scan area size. This scale-dependent rms roughness $R_{rms}(L)$ is dependent on the scale L according to a power law of $R_{rms}(L) \propto L^{\alpha}$, where α is called roughness exponent[76]. The value of α can be estimated from the slope of a scale-dependent part in the curve, and α was approximately 0.6 for the films in cubic phase growth stage. For the films in initial layer growth stage and transition stage, α ranged from 0.3 to 0.6. Roughness exponent α in the range of $0< \alpha <1$ suggests anisotropic scaling, and BN film surfaces are thus identified as self-affine fractal[76]. Similar analyses of the films prepared by vapor deposition[77,78] and the films sputtered by ion beam[75] often result in self-affine fractal, and in this point *c*BN film was not an exception.

In Fig. 3-4-2-2, the scale-independent rms roughness R_{rms} estimated from the above method was plotted against deposition time. R_{rms} ranged from 0.3 nm to 0.9 nm while that of a pre-sputtered silicon substrate was below 0.2 nm. Kinetic roughening in the surface of growing *c*BN film and smoothing feature after cubic phase formation are apparent in Fig. 3-4-2-2.

Scaling theory predicts a correlation of $R_{rms} \propto t^{\beta}$ for the films grown in a single process, where β is called growth exponent[76]. In our case, three regions (roughening-smoothing-roughening) revealed in Fig. 3-4-2-2, corresponding to each growth stage, and β was unable to set to a single value throughout the *c*BN film growth. But for the film with deposition time longer than 150 s showed stable growth, and growth exponent β was estimated to be about 0.6. In this stage, *c*BN film is considered to grow in a single growing process, which is consistent with the result of roughness exponent mentioned above. The surface smoothing after cubic phase formation was also reported in the growth of *c*BN film by low pressure inductively coupled plasma enhanced chemical vapor deposition[68], and the surface smoothing and subsequent roughening during film growth was also reported in growth of polysilicon by low pressure chemical vapor deposition[79], though their origin is unknown. The lateral growth of locally nucleated- and separated- *c*BN grains might have resulted in this smoothing.

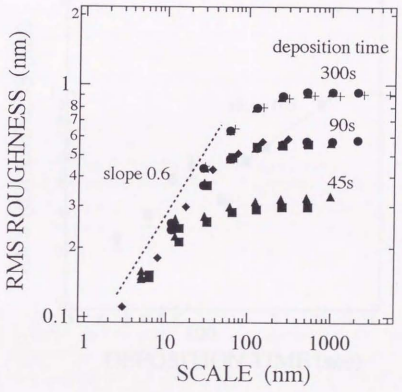

Figure 3-4-2-1 Scale dependent rms roughness calculated from AFM height data of the films deposited for 45 s, 90 s and 300 s. Scan size : cross (5 μm × 5 μm), circle (2 μm × 2 μm), triangle (1 μm × 1 μm), square (500 nm × 500 nm) and rhombus (300 nm × 300 nm).

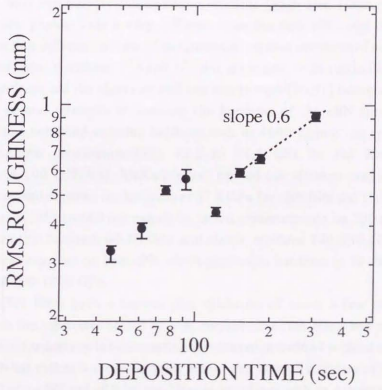

Figure 3-4-2-2 Time evolution of scale independent rms roughness during *c*BN film deposition process.

3.5. Nanoindentation measurements

Recent progress in *c*BN film deposition enables *c*BN film coating to various substrates, but whether these vapor deposited *c*BN film is as hard as bulk *c*BN or not is a question. Regardless of various ion-assisted vapor deposition methods applied to *c*BN film deposition[80,81,82,83,84,85,86,87,88,89], most of the obtained films were thin (thickness in order of 100 nm) and polycrystalline/nanocrystalline (grain size 10nm～100nm), and contained non-cubic phases. This is very different from the bulk *c*BN, and the mechanical properties may be thus different. In case of nanoindentation measurements of natural diamond and CVD diamond films (thickness: 125 and 375 μm, grain size: ～20 μm in diameter), it was found that the hardness and the elastic moduli was nearly equal[90,91] between them.

There are several attempts to measure the hardness of the *c*BN films. The vapor deposited *c*BN films exhibited extreme hardness such as 4000 kg/mm^2 as obtained by the micro-Vickers hardness measurement[92], 42.2 to 61.8 GPa for the Knoop hardness measurement (load 100 mN)[93]. McKenzie[94] carried out ultralow load (load 10 mN) indentation testing, and obtained the hardness of 57.6 GPa for *c*BN film and 19.6 GPa for *h*BN film. Mirkarimi *et al.*[95] carried out nanoindentation measurements on 700 nm thick *c*BN film, and obtained the hardness 60-80 GPa and elastic modulus 470-590 GPa. They also performed the measurements on bulk *c*BN which resulted in hardness of 40-70 GPa and the elastic modulus of 700-1000 GPa.

Since the *c*BN films have a limited film thickness of about a few 100 nm due to delamination from the substrates caused by high compressive film stress and poor adhesion, the measurement of hardness by the conventional indentation method without substrate effect is very difficult. What makes it more complex is that the layered structure of the *c*BN films consists of initial non-*c*BN and *c*BN layers. Nanoindentations with an extremely low load, a highly sharp tip and an extremely shallow penetration depth along with additional structural analyses are necessary to study the mechanical properties of such films. In this study, nanoindentations using a cube-corner shaped diamond tip were tried to study the mechanical properties of *c*BN films. To study the effects of the layered structure on the mechanical properties, *c*BN films in different growth stages were examined. The dependence of evaluated hardness and elastic modulus on film thickness and penetration depth were discussed in correlation with the layered structure of the *c*BN films.

Nanoindentations were carried out with a transducer (Triboscope, Hysitron) equipped AFM (Nanoscope III, Digital Instruments) shown in Figure 3-5-1 (a) under ambient conditions. Surface imagings and indentations were performed with the same tip. Indenting locations were carefully chosen by surface imagings so that the indents were always made at fresh places with no irregular deposits. A diamond tip with a triangular based cube-corner shape was mainly used in this study. Its geometry is shown in Figure 3-5-1 (b). It had a half angle of 35.2 degrees and

a total included angle of 90 degrees. The tip was acute compared to the most commonly used Berkovich tip, a triangular pyramid with the same depth-area relation as the standard Vickers indenter (square pyramid), which has a half angle of 65.3 degrees and a total included angle of 142.2 degrees. The cube-corner tip penetrated deep into the specimen and induced plastic deformation with a very low load compared to the Berkovich tip because of its tip geometry.

The largest difference between conventional hardness test and nanoindentation is the definition of hardness. In the former test, the hardness is determined as load divided by plastically deformed area, and one needs to observe the area of residual-plastic-indents. In this case, if there is only an elastic deformation, the hardness is not able to be determined. In the latter test, commonly used determination of hardness is the load divided by contact area between the indenter and the film at the maximum load, which is evaluated by the load-displacement relationship recorded during the indentation. In this case, the "elastic" hardness can be measured, and additionally, elastic modulus can be evaluated. For relatively soft, ductile materials such as metals, the former measurements is effective, but the observation of the residual indents become difficult as the load is decreased for the thin film measurements. For hard, brittle material such as ceramics, large elastic recovery and brittleness makes the observation of residual indents difficult. In this study, the hardness and elastic modulus were evaluated from the loading-unloading curves by the method described by Oliver *et al.*[96]. Since Poisson's ratio for the film was unknown, the elastic modulus were evaluated in the form of $E/(1-\nu^2)$. The elastic modulus (76.2 GPa) and Poisson's ratio (0.14) for a quartz glass (T-1030, Toshiba Ceramics) was used for contact area calibration. For measurements with cube corner tip, maximum loads were varied from 5 μN to 400 μN and the loading rate was set constant at 2 μN/s.

3.5.1. Difference in residual indents

Fig. 3-5-1-1 shows the AFM images of residual indentations obtained after a series of indentations with three different maximum loads (30 μN, 100 μN, 300 μN) to a silicon wafer and the *c*BN films in different growth stages. The z range of the images is set narrow so that the shape of residual indentations will be clearly shown. For the silicon wafer, the residual indentations were observed for indentation with a maximum load as low as 5 μN, and pile-ups were observed. The area of residual indentations decreased as the *c*BN film grew thick, which indicates the increase in hardness of the specimen by *c*BN film coating. For specimens with only an initial layer, the indents were comparable with those of the silicon wafer, but the pile-ups were smaller. For specimens with a thick *c*BN layer, the area of residual indentations decreased drastically and indentations with low maximum loads did not result in any residual indentations.

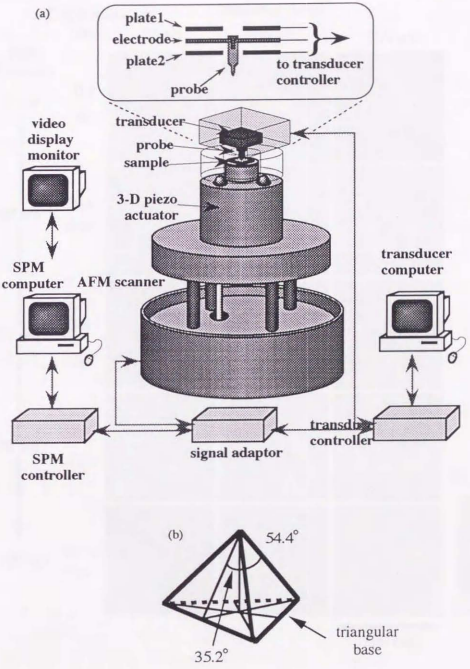

Figure 3-5-1 (a)Schematic diagram of nanoindentation apparatus and (b) the geometry of the cube corner tip.

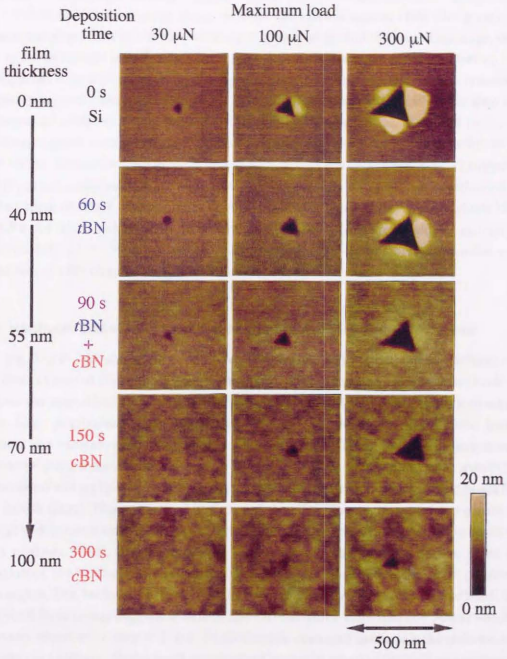

Figure 3-5-1-1 AFM images of the residual indentations observed using a indentation tip on a silicon wafer and the *c*BN films in different growth stages.

3.5.2. Change in load-unload curves

Figure 3-5-2-1 shows the loading-unloading curves obtained for a silicon wafer and the *c*BN films in different growth stages by indentations with a constant maximum load of 100 μN. The decrease in the penetration depth was not monotonic against *c*BN film growth. The decrease was slight for films in the initial layer growth stage and the transition stage, but for films in the cubic layer growth stage, there was a substantial decrease in the penetration depth. It is apparent from the curves that the deformations of the films as a result of the indentations changed from partly elastic to completely elastic deformations as the *c*BN layer grew thick. The degree of elastic recovery defined as the elastic deformation depth divided by the total deformation depth increased from 0.4 (silicon wafer, $t = 0$ s) to 1.0 ($t = 300$ s) in this series of indentations. Circular residual indentations at a low maximum load in Fig. 3-5-1-1 suggest that the tip was not completely sharp and had a finite radius. The tip radius can be estimated from the load curve of elastic indentation[97]. Assuming that the reduced elastic modulus is 200 $\sim$ 400 GPa for the thickest *c*BN film (t = 300 s), the tip radius could be estimated as approximately 12 $\sim$ 50 nm from the curve in Fig. 3-5-2-1, which is comparable to the crystal size of *c*BN observed in the TEM study.

3.5.3. Hardness and elastic modulus evaluated from load-unload curves

Fig. 3-5-3-1 (a) shows the contact depth dependence of the normalized hardness of the *c*BN films evaluated from the loading-unloading curves with various maximum loads. The hardness was normalized with 12 GPa, which was the evaluated hardness of the silicon substrate in the large penetration depth region. Fig. 3-5-3-1 (b) shows the normalized hardness evaluated at a constant contact depth of 15 ± 3 nm for *c*BN films in different growth stages. The normalized hardness increased slightly for the *c*BN films in the initial layer growth stage, and increased almost lineary as *c*BN formed (transition stage) and grew in single phase (cubic layer growth stage). The normalized hardness of the *c*BN films in the cubic layer growth stage was highly dependent on the contact depth. This dependence on the penetration depth is due to the substrate effect, and the evaluated hardness is not the hardness of film alone since saturation of the hardness (plateau in the curve) was not observed in the small penetration depth region. The hardness of thick *c*BN films was affected by a soft substrate and a soft initial sp^2-bonded layer comprising about half of the 110-nm-thick *c*BN film ($t = 300$ s) which was previously observed in chapter 3-2-1. Therefore the evaluated hardness is the underestimated combination hardness. Similar trend was observed in case of nanoindentation measurements of amorphous carbon films deposited on silicon substrates[98].

Fig. 3-5-3-2 (a) shows the contact depth dependence of the normalized elastic modulus. The elastic modulus was normalized with 170 GPa, which was the evaluated elastic modulus of the silicon wafer at the large penetration depth region. Fig. 3-5-3-2 (b) shows the normalized elastic modulus evaluated at a constant contact depth of 15 ± 3 nm for *c*BN films in different growth stages. The evaluated elastic modulus decreased as the initial layer grew, which

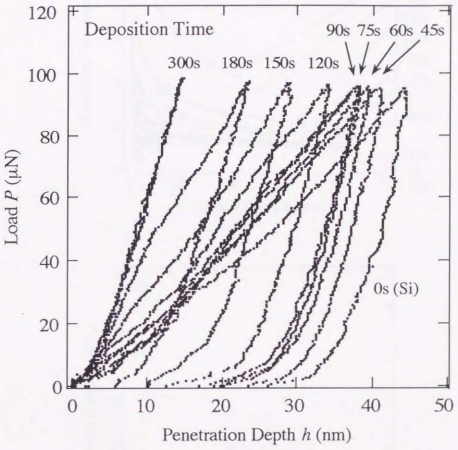

Figure 3-5-2-1 Loading-unloading curves of the cBN films in different growth stages. The maximum load was 100 μN.

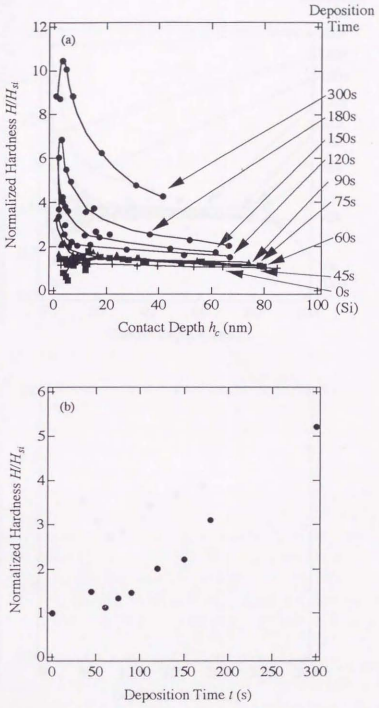

Figure 3-5-3-1 (a) Contact depth dependent normalized hardness of cBN films in different growth stages. The hardness was normalized with 12 GPa, which was the hardness of a silicon wafer at the large penetration depth region. (b) Deposition time dependent normalized hardness evaluated at contact depths of 15±3 nm.

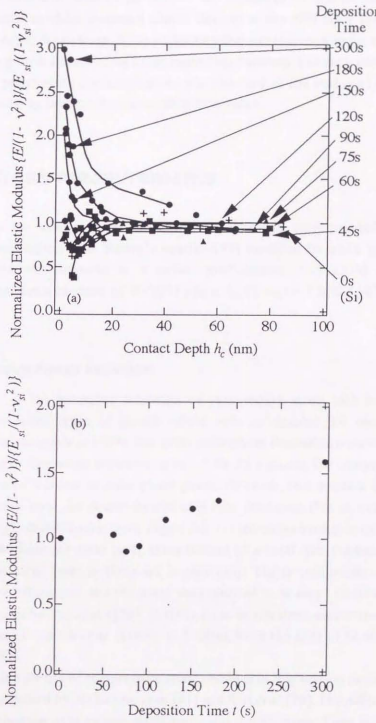

Figure 3-5-3-2 (a) Contact depth dependent normalized elastic modulus of cBN films in different growth stages. Elastic modulus $E/(1-\nu^2)$ was normalized with 170 GPa, which was the elastic modulus of a silicon wafer at the large penetration depth region. (b) Deposition time dependent normalized elastic modulus evaluated at contact depths of 15 ± 3 nm.

reflected the low elastic modulus of sp^2-bonded BN compared to that of the silicon wafer substrate. The elastic modulus increased almost linearly as the *c*BN layer formed and grew. The penetration depth dependence of the evaluated value was also obvious for thick *c*BN films in the cubic layer growth stage, similar to the case of the hardness. The saturation of the elastic modulus at small penetration depth region was not observed, so the evaluated elastic modulus of *c*BN film was also an underestimated combination value.

3.6. Film stress measurements

Film stress was evaluated by measuring the substrate curvature before and after deposition, and employing it to Stoney's equation[99] modified for plate geometry[100]. Substrate curvature was measured by a surface profilometer (SURFCOM 470A, Tokyo Seimitsu). Reduced elastic modulus of Si (100) plane, $E_{Si}/(1-\nu_{Si}) = 1.805 \times 10^{11}$ Pa, was cited from Ref.101.

3.6.1. Compressive stress evolution

Figure 3-6-1-1 (a) shows the evolution of compressive stress with increase in film thickness. In the initial stage of growth where only sp^2-bonded BN was growing, the compressive stress was as low as 1 GPa. But as the cubic phase formation occured and film grew further, compressive film stress increased up to 5 GPa. At a glance, the compressive stress in cubic phase seems to increase as cubic phase grows. However, this increase is the result of evaluating film stress over the double-layered *c*BN film thickness, that is, over low-stressed initial layer and high-stressed cubic layer. Figure 3-6-1-1 (b) shows evolution of calibrated film stress using the thickness of cubic layer alone instead of a total film thickness. This result clearly shows that cubic layer in films are in equivalent highly compressive stressed state independent of their thickness, and the stress was evaluated to be about 10 GPa which is close to the value evaluated by Ilias *et al.* ([70], 11 GPa), from *in-situ* stress measurements during the film deposition, and Friedrich *et al.* ([102], 11.5 GPa), from the shift of IR absorption peak associated with *c*BN.

The evolution profile of compressive stress obtained in this study is somewhat different from the profile obtained by McKenzie *et al.*[41] and Ilias *et al.*[70]. The difference is mainly due to the determination of thickness dependent compressive stress. They studied the stress evolution inside the film, and evaluated stress using grown film thicknesses[41] and etched depths[70]. McKenzie *et al.* carried out *in situ* stress measurement during the ion plating deposition of a *h*BN film. The obtained profile showed sharp increase at the initial stage of the deposition followed by decrease to a plateau value. Ilias *et al* carried out stress measurements during the reactive ion etching (in a gas mixture SF_6:O_2) of a *c*BN film. They found that the stress sharply increased to maximum value of 17 GPa (the average was 12 GPa) inside the

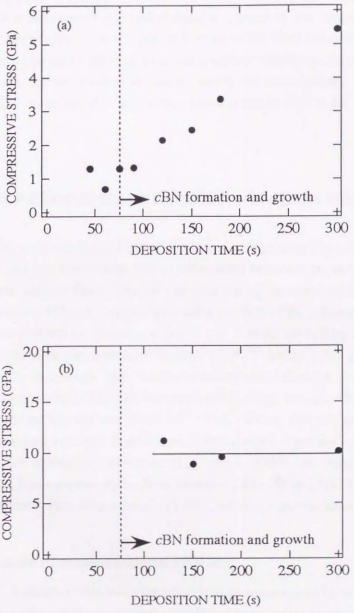

Figure 3-6-1-1 The dependence of compressive stress on the phase evolution in *c*BN film deposition process. The stress was evaluated using (a) a whole film thickness and (b) a *c*BN layer thickness alone, respectively.

initial *h*BN layer, then the stress relaxed at the mixed zone of *c*BN and *h*BN, and finally it increased to nearly homogeneous highly compressive value of 11 GPa in the major part of the *c*BN layer. Cardinale *et al.*[103] measured the residual stress of *c*BN films by cantilever beam deflection method. They prepared thin substrate (10-15 μm) by micromachining and thus relatively accurate measurement of small deflection caused by low stressed film and high stressed thin film was possible. The compressive stress of BN films lied in the range of 0.15 to 5.5 GPa. From the compressive stress data and the evaluated elastic constants of *t*BN and *c*BN, they considered that the ion irradiation induced nearly the same amount of strain (0.5 %) in*t*BN layer and *c*BN layer, and the large compressive stress in *c*BN is due to its high elastic modulus.

3.7. Cross-sectional transmission electron microscopy

Specimens for cross-sectional TEM observations were prepared by a standard technique. Two silicon wafer and two film coated silicon were cutted in same size, and piled into a piece with epoxy between each of them. Then it was sliced using diamond cutter into five or six pieces with thickness of 750 μm, and polished using powders of SiC, diamond and alumina in sequence until it was thinned to thickness under 50 μm. Finally ion milling was applied to the specimens using Precision Ion Polishing System (PIPS^{TM} Model 691, gatan) before the observation. Atomic resolution high voltage transmission electron microscope (JEM-ARM1250, JEOL) operating at 1250 kV was employed for high resolution TEM observations. The stability of applied voltage was about $10^{-6} \sim 10^{-7}$ V/min, and the exposing time was controlled to be less than 1 second. The lens coefficients were 1.6 mm for spherical aberration (C_s) and 4.0 mm for chromatic aberration (C_c), which enable the resolution of 0.1 nm. Cross-sectional EELS was performed by field emission TEM (JEM-2010F) operating at 200 kV. Analysing specimen areas were as small as 1 nm^2, while energy resolution was about 0.7 eV.

3.7.1. Microstructure of cross-sectional *c*BN film

Figure 3-7-1-1 shows a wide area high resolution cross-sectional TEM image of the *c*BN film. In Fig. 3-7-1-1, the substrate adjacent amorphous layer, intervening *t*BN layer and *c*BN layer were cleary observed, which is similar to the structure previously reported in Ref. 56, 57, 58, 59, 60 and 61. Inserted images in Fig. 3-7-1-1 are representative enlarged images from the *c*BN layer and the *t*BN layer respectively. The *t*BN layer showed orientation with its *c*-axis nearly pararell to substrate surface. The interface between *t*BN layer and *c*BN layer was rough compared to the growing surface which was measured by tapping AFM, and this result supports the simultaneous growth of the two phase.

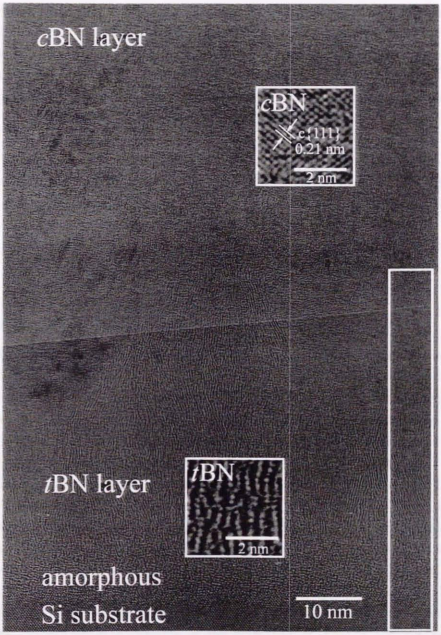

Figure 3-7-1-1 Wide-area high-resolution cross-sectional TEM image of the *c*BN film deposited on a silicon substrate. Inset enlarged images are representative images of the *c*BN layer and the *t*BN layer.

3.7.2. Phase identification using electron energy loss spectroscopy

Cross-sectional TEM image and electron energy loss spectra near B K-edge obtained by FE-TEM are shown in Fig. 3-7-2-1. The TEM image shows double-layered structure consisted of dark contrast layer near the substrate and bright contrast layer above the dark layer. Epoxy and part of the bright layer seem to be sputtered away during ion milling, which resulted in an amorphous layer at the top of the bright layer. Points where EELS spectra were taken are marked in the image. Near edge structures of B K-edge spectra consisted of sharp π^* line, broad σ^* line and additional sharp line. These lines can be used as a fingerprint of the bonding state of boron nitride[24]. π^* line is characteristic for spectra obtained from pure *h*BN, while additional sharp line is characteristic for pure *c*BN[24]. Spectra from the dark layer (4,5,6) had strong π^* line due to sp^2-bonded BN, and this layer was identified as the initial sp^2-bonded BN layer. Spectra from the bright layer (1,2,3) had additional sharp line, and thus this layer was identified as the *c*BN layer. The spectra from the bright layer had slight π^* line, but considering the result of IR measurements, the line may arised from sp^3 to sp^2 conversion by ion milling rather than coexistence of sp^2-bonded BN and *c*BN. By using EELS with electron beam size as small as 1 nm^2, phase identification of these layers were able to directly carried out.

3.7.3. Observation of *c*BN nucleation site on initial layer

High magnification cross sectional TEM image of *t*BN/*c*BN interface observed by high voltage TEM is shown in Figure 3-7-3-1. The arrow beside the image indicates the growing direction of the film. It is apparent from the image that *t*BN grew with *c*-axis nearly parallel to the substrate surface. At the very interface, two *r*BN{00*l*} planes matching up with three *c*BN{111} planes were observed. This orientation relationship is similar to the case of diamond nucleation on highly oriented pyrolitic graphite (HOPG)[104] and to the case predicted for pressure induced direct diffusionless conversion of *r*BN into *c*BN[29]. Similar relationship was also observed by Medlin *et al.*[105] and Reinke *et al.*[106]. Two-dimensional Fast Fourier Transformation (FFT) of the image was performed in order to analyze crystal structure inside the *t*BN layer. The result is also shown in Fig.3-7-3-1, and from angular and distance relationship, the spots were identified as *r*BN{003}, *r*BN{101} and *r*BN{102} respectively. Similar diffraction spots were reported in Ref. 107 for *r*BN whisker. However, a pair of innermost spots showed broadening which was attributed to both local change in plane distance and distribution in orientation of BN atomic layer. This broadening indicates the coexistence of *r*BN and *t*BN. Evidence for the presence of *r*BN in BN film deposited by ion-assisted pulsed laser deposition was previously presented by Medlin *et al.*[108]. They observed three-layer stacking in a plan-view HRTEM image of *t*BN in a BN film, and suggested that *r*BN would provide a low energy path in stress-induced formation of *c*BN. The structure and the orientation relationship observed in our study are consistent with the stress-induced formation of *c*BN from *r*BN, but whether *r*BN acts as a structural precursor or a preferred nucleation site remains unclear. However, *r*BN appears to have strong effect on *c*BN formation and its crystal

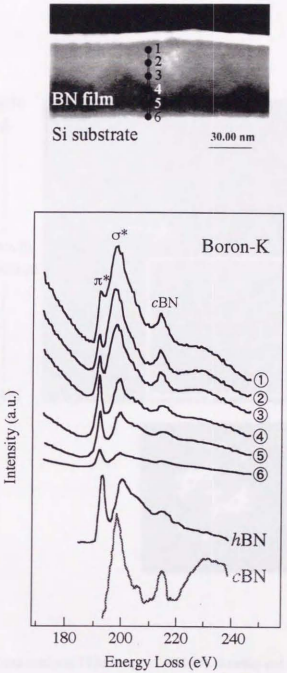

Figure 3-7-2-1 A cross-sectional TEM image and electron energy loss spectra near B K-edge obtained by FE-TEM operating at 200 kV. Analysing points are shown in the image. Boron-K edge energy loss spectra for pure *h*BN and *c*BN are quoted from Ref. 24.

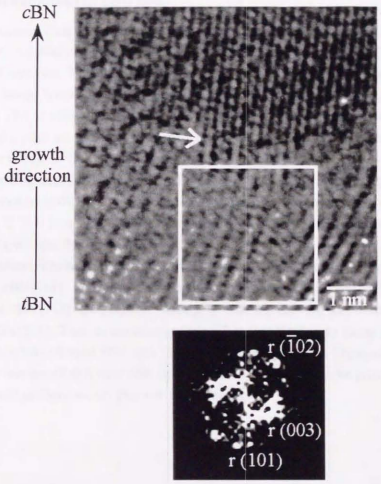

Figure 3-7-3-1 Cross-sectional TEM image of *t*BN/*c*BN interface and Fourier transformed figure. TEM image was observed by atomic resolution high voltage electron microscope. Fourier transformation was applied to image surrounded by white square frame. White arrow indicates the very interface where two $t\{00l\}$ planes match up with three $c\{111\}$ planes.

size and orientation. The study on the origin of *r*BN stacking formation in *t*BN layer should lead to the controlled *c*BN formation.

3.7.4. Structural evolution of *c*BN film

Two-dimensional Fourier transformation along the cross-sectional TEM image was performed in order to obtain the diffractional information and analyze the film thickness dependent crystal structure. Figure 3-7-4-1 shows a series of results which corresponds to the gradual structure change from silicon substrate (Fig. 3-7-4-1(h)), amorphous(Fig. 3-7-4-1(g)), *t*BN (Fig. 3-7-4-1 (f)) to *c*BN (Fig. 3-7-4-1 (a)) during the *c*BN film growth. The TEM images in Fig. 3-7-4-1 is a part of the *c*BN film, which the same place is surrounded by a white rectangular frame in Fig. 3-7-1-1. The Fourier transformation result of Fig. 3-7-4-1 (e) was particularly interesting because it showed the *r*BN configuration. The broadening of innermost spots were attributed to both local change in plane distance and in orientation of BN atomic layer. So in Fig. 3-7-4-1 (e), *t*BN coexisted with *r*BN. The *r*BN configuration was only observed in *t*BN layer near the *c*BN nucleation sites.

The orientation relationship of *r*BN and *c*BN was also interesting. In Fig. 3-7-4-1 (d), fine spot from *c*BN{111} appeared near spots from *r*BN{101}, and *r*BN{101} spot disappeared as the *c*BN{111} spot became strong. Similar correlation was observed between *r*BN{003} and *c*BN{111}. This orientation relationship was similar to those predicted for direct diffusionless conversion of *r*BN into *c*BN at high pressure[109]. The result suggests the possibility of conversion of *r*BN into *c*BN upon initial layer, however, the possibility of *r*BN acting as a preferred nucleation site can not be neglected.

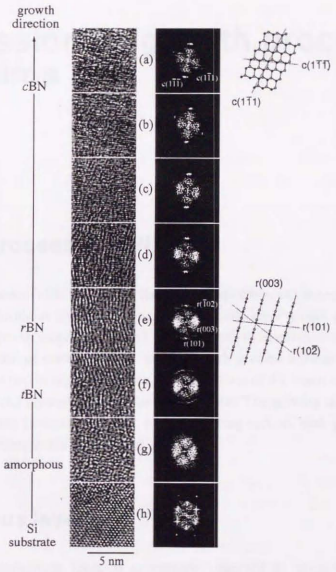

Figure 3-7-4-1 A cross-sectional TEM image of the *c*BN film devided in eight square parts and two-dimensional FFT results of each square images. The cross-sectional image is from a part surrounded by white rectangular frame in wide-area high-resolution cross-sectional TEM image shown in Fig. 3-7-1-1.

4. Discussion on growth process of *c*BN films

4.1. Growth process of *c*BN films

The growth process of *c*BN films in RF bias sputter deposition can be separated into four growth stages, i. e., amorphous layer growth stage, turbostratic layer growth stage, transition stage and cubic layer growth stage. This growth process seems to be a common process among *c*BN films grown by various methods. Since similar growth process is observed in methods which differ by order of two in deposition rates, the fluctuation of the vapor conditions is not an intrinsic origin for the layered structure of the *c*BN film. The growing surface condition should be satisfied for the formation of *c*BN. In the following section, each growth stage and corresponding layer structure will be discussed.

4.2. Amorphous layer

Existence of amorphous layer is commonly observed in cross-sectional TEM observation of *c*BN film. In case of our film, the thickness measured from the cross-sectional image (Fig. 3-7-1-1) was about 2 nm. This value is not special among the commonly reported values in range of 2-7nm[38,46,56,57]. This amorphous layer has been observed in almost every sample which was observed by cross-sectional TEM image, independent of substrate, independent of deposition process. However, there was one special case reported by Hoefsass *et al.*[60], in which this layer was not observed. The substrate in their experiment was a *c*BN film. So, the role of the amorphous layer is considered to be the preparation of proper surface for the crystalline BN growth, which contains no contaminants such as substrate atoms.

4.3. Intervening *t*BN layer

4.3.1. Orientation

Turbostratic layer was oriented with *c*-axis neary parallel to the substrate surface in our film. This characteristic orientation of the *t*BN layer i.e., BN atomic layers growing nearly perpendicular to the substrate surface, was also observed by other researchers [56,57,58,59,60,61]. The oriented *t*BN layer seems to provide a preferential nucleation site for *c*BN, similar to the case of diamond nucleation on a prism plane of highly oriented pyrolitic graphite (HOPG)[104,110]. Similar oriented graphitelike turbostraticlike layer was also found in CN_x film deposited by reactive magnetron sputtering[111] and ion irradiated glassy carbon[112].

Since the film stress of the initial layer averaged over the film thickness was about 1 GPa, and the local stress and/or the stress before relaxiation are possibly higher, the stress and the difference in compressibility between *a*-axis direction and *c*-axis direction of *t*BN[113] is considered to be the cause of the orientation. Roeder *et al.*[114] observed the influence of bias voltage on the orientation of the *h*BN film deposited by RF magnetron sputtering using cross-sectional HRTEM. They reported that when the film was deposited without external bias voltage, the *c*-axis of *h*BN lied perpendicular to the substrate surface, which was very different from the film deposited with negative bias voltage higher than 50 V exhibiting preferred orientation of *c*-axis parallel to the substrate surface. Since high negative bias voltage supplies energetic ions which generates compressive stress by atomic peening, their result is consistent with the stress-induced orientation model. Cardinale *et al.*[115] analyzed the relative thermodynamic stabilities of strained *h*BN and *c*BN single crystal structures for all orientations of biaxial stress and strain fields relative to the crystallographic directions using elasticity theory and the published values of the elastic constants. They found that in *h*BN, the most thermodynamically stable orientation is BN atomic planes oriented roughly 45° relative to either the biaxial plane of stress or strain. For *c*BN, they found that the stable orientation differed for the constant stress (<100> texture) or constant strain (out-of-plane <111> texture) assumptions. These textures are different from the observed texture, so the crystal orientation are not able to be explained in terms of elasticity. It seems reasonable to explain the orientation in terms of difference in compressibility of *t*BN and the film stress.

4.3.2. Formation of *r*BN in *t*BN layer

Clear evidence for the existence of *r*BN at the *c*BN nucleation site on *t*BN layer was obtained by FFT of cross-sectional TEM image in Fig. 3-7-3-1. In the enlarged image of the *t*BN layer in Fig. 3-7-1-1, bending and elimination of BN atomic layers were apparent, and the stacking sequence of BN atomic layers was highly disordered. This may be due to the high compressive stress formed in the film by ion bombardment during the growth. Similar structure

was observed by Horiuchi *et al.* in case of *h*BN to *c*BN transition under high pressure (7.7 GPa) and high temperature (1800 ℃)[116]. They observed the bending and the elimination of BN atomic layers at the site where folding of platelike crystal occured by external stress and/or volume shrinkage due to the formation of *c*BN grains. They also found that the local stacking sequence of the BN atomic layers in shrunk area is similar to that of *r*BN, and considered that BN atomic layer elimination could be one of the causes. Similar bending and elimination of BN atomic layers during the initial layer growth of *c*BN film might be one of the cause of the formation of *r*BN in ion-assisted vapor deposition.

4.3.3. Origin of thickness

*c*BN films on various substrates often results in a layered structure consisting of a substrate adjacent initial sp^2-bonded BN (*a*BN + *t*BN) layer and a sp^3-bonded BN (*c*BN) layer [56,57,58,59,60,61,68]. The layered structure is independent of processes such as ion beam assisted evaporation [56,61], ion-assisted pulsed laser deposition[57], RF bias sputtering[58], ion plating[59], mass separated ion beam deposition [60] and ICP-CVD[68]. However, initial layer thickness varies from a few nm([56], 2-5 nm)[60], a few tens of nm [57] ([58], 20 nm) ([59], 50 nm) ([61], ~10 nm) [68] ([117], 15 nm)to 100 nm[68] depending on the deposition process and experimental conditions. There is only one report on the observation of *c*BN crystallites forming near the substrate (β-SiC) partly without the intervening *t*BN layer[118]. These results suggest that *c*BN formation requires certain growing-surface condition(s) which is(are) satisfied after the growth of the sp^2-bonded BN layer to a certain thickness. McKenzie *et al.*[41] and Kester *et al.*[46] suggested that the presence of an initial layer with a considerable thickness is required to build up sufficient compressive film stress for *c*BN formation, but the stress-induced formation of *c*BN in the vapor deposition process is still ambiguous. FFT applied to the TEM images of initial layer along the growing direction (Fig. 3-7-4-1) showed no evidence for *r*BN near the substrate, at the "initial growth stage" of the *t*BN layer. *r*BN seems to form as a result of the initial layer growth to a critical thickness. Formation of *r*BN, rather than building up of the stress seems to be the origin of the critical initial layer thickness.

4.4. Formation of cubic phase on *t*BN layer

4.4.1. Orientation relationship between *c*BN and initial layer

At the nucleation site of *c*BN on *t*BN(*r*BN), two *t*BN{00*l*} or *r*BN {003} planes matching up with three *c*BN{111} planes were observed. Similar relationship was also observed by Medlin *et al.*[105], Reinke *et al.*[106] and Zhou *et al.*[119, 120]. Two-dimensional FFT of cross-sectional TEM images revealed the orientation relationship between *r*BN and *c*BN, i.e.,

correlation between *r*BN{101} and *c*BN{111}, and between *r*BN{003} and *c*BN{-1-1-1}, which was similar to the relationship of diamond nucleation on highly oriented pyrolitic graphite (HOPG)[104] and to the case of pressure-induced direct diffusionless conversion of *r*BN into *c*BN[29]. The direct diffusionless conversion of *r*BN to *c*BN is reported to occur in shock-compression[29] and static-compression[30] of *r*BN. Interesting point is that this transition path has low activation energy which was estimated by an *ab initio* study([109], 0.38 eV/pair), compared to the activation energy along the transition path from *h*BN to *c*BN ([12], 8.7 eV). If this is the process occuring at the nucleation site of *c*BN, the formation of *c*BN is a low-temperature stress-induced process, but this study could not determine the exact role of *r*BN. To reveal the role and formation mechanism of *r*BN, further study is necessary.

4.4.2. Nucleation density

Comparing the *c*BN/*t*BN interface roughness observed in cross-sectional TEM image and the growing surface roughness measured from tapping AFM image, local nucleation and simultaneous growth of *t*BN phase and *c*BN phase was revealed. IR analysis and XPS analysis also support the existence of this growth stage. Coexistence and simultaneous growth of the two phases were also reported by Barth *et al.*[69] and Ilias *et al.* [70]. This means that sp^2-bonded phase and sp^3-bonded phase grow in same depositing particle condition, but the growing phase depends on the surface condition. The crystal size is determined by the coalescence of neighboring *c*BN crystals, that is, by the distance of nucleation site. Since the commonly reported *c*BN grainsize is about 20 nm, the nucleation density of *c*BN over initial layer is estimated to be about $3 \times 10^{15}/m^2$. This value is approximately equal to the density of grainlike structure observed in AFM image of initial layer in Fig. 3-4-1-1 (a). It will be significant to study whether the grainlike structure itself or the boundary of grainlike structure act as a nucleation site of *c*BN. If *c*BN nucleation occurs from the sp^3 bonds which lie at the boundary of *t*BN grains like the model proposed in sp^3 bond formation in turbostratic carbon[121], control of *t*BN grain size will lead to the deposition of *c*BN films with larger crystal size.

4.5. Single phase growth of *c*BN layer

4.5.1. Orientation

Considering the result of structural evolution from *r*BN to *c*BN, the orientation of *c*BN layer seems to be dependent on the orientation of initial *t*BN layer. Preferred orientation of <110> axis of *c*BN parallel to growing direction has been reported by several groups [58, 122, 123]. They attribute the origin of this orientation to the nonpolar nature (equivalent atomic density of boron and nitrogen). By studying the azimuthal variations in the diffraction taken

from the film, Medlin *et al.*[108] observed that the *c*BN crystallites are preferentially oriented with at least one [111] direction lying in the plane of film but otherwise random. They considered the previously reported preferred orientation of <110> axis of *c*BN parallel to growing direction was the special case of their finding. Their result is consistent with our observed relationship between rBN{003} and *c*BN{111}, and the orientation of *r*BN.

4.5.2. Growing surface

The phase existing at the growing front of *c*BN film is an important information in search for *c*BN formation and growth mechanism. Friedmann *et al.*[38], performed *in situ* AES measurements on films deposited with and without the ion beam assistance during the pulsed laser deposition of BN film. The boron KVV line shape both obtained from irradiated region (*c*BN containing region) and unirradiated (no *c*BN containing region) most closely matched to the reference spectrum obtained from *h*BN/*t*BN, which suggests the growing surface of *c*BN film is *h*BN/*t*BN, and the conversion to *c*BN occurs below the surface. Dworschak *et al.*[124] calculated difference between the number of interstitials and vacancies created by ion bombardment as a function of depth from film surface using the TRIM computer program. They found that with 500 eV argon ion bombardment of *h*BN, the largest density increase occurs at 2 nm below the surface. This result is considered to be consistent with the result obtained by Friedmann *et al.*[38], and the subplantation model for *c*BN formation. But since TRIM program is for amorphous material, and the ion bombardment is to the static surface, it is believed to be not sufficient enough to be applied to the crystalline material (even if it is nanocrystalline) like *c*BN film and dynamic process like *c*BN formation. Park *et al.*[125] also observed the π bond shake-up satellite peak in XPS spectra of the *c*BN film as they increased the surface sensitivity by increasing the take-off angle. From the intensity variation of the π bond shake-up satellite peak with take-off angle and the electron mean free path value in *h*BN matrix (they estimated as 3.0 nm), the thickness of *h*BN layer at the top of *c*BN film was estimated to be about 1.2 ± 0.2 nm, which is close to the depth of most densified layer calculated by Dworschak *et al.*[124]. However, their B 1s XPS spectra of thick *c*BN film obtained at the substrate normal already showed a slight feature of π bond shake-up satellite peak, so there is a possibility that their film was not completely covered with *c*BN phase. Sene *et al.*[126] and Ilias *et al.*[70] observed an evidence for existence of 3-4 monolayers of *h*BN on top of *c*BN film synthesized by ion beam assisted evaporation of boron, using reflection electron energy loss spectroscopy (REELS).

In this study, angle resolved XPS was applied to the *c*BN film. The angle was increased to 70 degrees, so that the surface BN layer with thickness of only 0.5-0.7 nm would attribute to the signal. As a result, no evidence for the existence of sp^2-bonded phase was observed. This result is consistent with the difference in tip-surface interaction observed in contact AFM observation of films in different growth stages. Even if there exists a layer of sp^2-bonded BN on top of the cubic layer, the thickness would be considerably small compared to 0.5-0.7 nm, and the structure would be different from the oriented *t*BN layer. The structure of surface layer

on top of *c*BN crystallites is thus considered to be different from the growing front of initial layer, and the growth mechanism and the formation mechanism should be considered separately.

5. Conclusions

This study concentrated on obtaining information on the growth of *c*BN film from vapor phase by characterizing the deposited film systematically. The results revealed following conclusions on *c*BN film growth process.

The growth process of *c*BN film in RF bias sputter deposition was separated into four growth stages, i. e., amorphous layer growth stage, turbostratic layer growth stage, transition stage and cubic layer growth stage.

In amorphous layer growth stage, an amorphous layer grows until it completely covers the substrate surface with boron nitride in order to prepare clean surface with no degrading contaminants for the crystalline BN growth.

In turbostratic layer growth stage, *t*BN grows with its BN atomic planes perpendicular to the substrate due to the compressive film stress, which is about 1 GPa. This layer provides the preferential nucleation sites for *c*BN. Although *t*BN is random in its stacking, it partly forms denser sp^2-bonded phase (*r*BN) during the growth through bending and elimination of BN atomic planes, and the ratio of denser sp^2-bonded phase to *t*BN seems to increase with the increase in layer thickness.

In transition stage, *c*BN nucleates on *r*BN in *t*BN layer, and simultaneously grows with sp^2-bonded phase. *c*BN nucleates in density about 3×10^{15} /m^2, which is near the density of *t*BN grains observed in AFM image. The orientation relationship between *r*BN and *c*BN can be characterized by the strong correlation between *r*BN{101} and *c*BN{111}, and between *r*BN{003} and *c*BN{-1-1-1}.

In cubic layer growth stage, *c*BN grains grow in single phase. The high compressive stress of 10 GPa is due to the high elastic constant along the in-plane axis. And it is not a cause but a result of the orientation of *c*BN layer, which is determined by the orientation relationship with the underlying *r*BN.

Although it is unclear whether *r*BN acts as a structural precursor or a preferred nucleation site, *r*BN in the initial layer seems to be strongly related to *c*BN formation. Revealing the exact role of *r*BN in *c*BN formation, and its formation mechanism and condition inside the initial layer will lead to the high quality *c*BN film.

Bibliography

1 C. A. Brookes, "The mechanical properties of cubic boron nitride - a perspective view", Inst. Phys. Conf. Ser. 75 (1986) pp. 207-219

2 T. Taniguchi, M. Akaishi and S. Yamaoka, "Mechanical properties of polycrstalline translucent cubic boron nitride as characterized by the Vickers indentation method", J. Am. Ceram. Soc. 79 (1996) pp. 547-549

3 E. Knittle, R. M. Wentzcovitch, R. Jeanloz and M.L. Cohen, "Experimental and theoritical equation of state of cubic boron nitride", Nature 337 (1989) pp. 349-352

4 G.A. Slack, "Nonmetallic crystals with high thermal conductivity", J.Phys. Chem. Solids 34 (1973) pp. 321-335

5 R. H. Wentorf, Jr., "Cubic form of boron nitride", J. Chem. Phys. 26 (1957) pp. 956

6 R. M. Chrenko, "Ultraviolet and infrared spectra of cubic boron nitride" Solid State Communications 14 (1974) pp. 511-515

7 R. F. Davis, "III-Vnitrides for electronic and optoelectronic applications", Proc. IEEE 79 (1991) pp. 702-712

8 R. H. Wentorf, Jr., "Preparation of semiconducting cubic boron nitride", J. Chem. Phys.36 (1962) pp. 1990-1991

9 O. Mishima, "Cubic boron nitride pn junction made at high pressure", Materials Science Forum Vols. 54&55 (1990) pp. 313-328

10 J. Thomas Jr., N. E. Weston and T. E. O'Connor, "Turbostratic boron nitride, thermal transformation to ordered-layer-lattice boron nitride", J. Am. Chem. Soc. 84 (1963) pp. 4619-4622

11 F. P. Bundy and J. S. Kasper, "Hexagonal diamond - A new form of carbon", J. Chem. Phys. 46 (1967) pp. 3437-3446

12 F. R. Corrigan and F. P. Bundy, "Direct transitions among the allotropic forms of boron nitride at high pressures and temperatures", J. Chem. Phys. 63 (1975) pp. 3812-3820

13 F. P. Bundy and R. H. Wentorf, Jr., "Direct transformation of hexagonal boron nitride to denser forms", J. Chem. Phys. 38 (1963) pp. 1144-1149

14 Q. Johnson and A. C. Mitchell, "First X-ray evidence for a phase transition during shock-wave compression", Phys. Rev. Lett. 29 (1972) pp.1369-1371

15 V.L. Solozhenko, "New concepts of BN phase diagram: an applied aspect", Diamond and Related Materials 4 (1994) pp. 1-4

16 V.L. Solozhenko, "Current trends in the phase diagram of boron nitride", J. Hard Mater. 6

(1995) pp. 51-65

17 K. Albe, "Theoretical study of boron nitride modifications at hydrostatic pressures", Phys. Rev. B 55 (1997) pp. 6203-6210

18 P. J. Gielisse, S. S. Mitra, J. N. Plendl, R. D. Griffis, L. C. Mansur, R. Marshall and E. A. Pascoe, "Lattice infrared spectra of boron nitride and boron monophosphide", Phys. Rev. 155 (1967) pp. 1039-1046

19 S. Fahy, "Calculation of the strain-induced shifts in the infrared-absorption peaks of cubic boron nitride", Phys. Rev B 51 (1995) pp. 12873-12875 ; S. Fahy, "Erratum: Calculation of the strain-induced shifts in the infrared-absorption peaks of cubic boron nitride [Phys. Rev. B 51, 12873 (1995)", Phys. Rev. B 53 (1996) p. 11884

20 R. Geick, C. H. Perry and G. Rupprecht, "Normal modes of hexagonal boron nitride", Phys. Rev. 146 (1966) pp. 543-547

21 R. A. B. Devine, "Structural nature of the Si/SiO_2 interface through infrared spectroscopy", Appl. Phys. Lett. 68 (1996) pp. 3108-3110

22 G. P. Lamaze, R. G. Downing, L. B. Hackenberger, L. J. Pilione and R. Messier, "Analysis of cubic boron nitride thin films by neutron depth profiling", Diamond and Related Materials 3 (1994) pp. 728-731

23 R. Trehan, Y. Lifshitz and J. W. Rabalais, "Auger and x-ray electron spectroscopy studies of hBN, cBN, and N_2^+ ion irradiation of boron and boron nitride", J. Vac. Sci. Technol. A 8 (1990) pp. 4026-4032

24 D. R. McKenzie, W. G. Sainty and D. Green, "The microstructure of boron nitride thin films", Mater. Sci. Forum 54&55 (1990) pp. 193-206

25 L. J. Terminello, A. Chaiken, D. A. Lapiano-Smith, G. L. Doll and T. Sato, "Morphology and bonding measured from boron-nitride powders and films using near-edge x-ray absorption fine structure", J. Vac. Sci. Technol. A 12 (1994) pp. 2462-2466

26 A. Chaiken, L. J. Terminello, J. Wong, G. L. Doll and C. A. Taylor II, "Electronic and atomic structure of metastable phases of boron nitride using core-level photoabsorption", Appl. Phys. Lett. 63 (1993) pp. 2112-2114

27 I. Jimenez, A. F. Jankowski, L. J. Terminello, D. G. Sutherland, J. A. Carlisle, G. L. Doll, W. M. Tong, D. K. Shuh and F. J. Himpsel, "Core-level photoabsorption study of defects and metastable bonding configurations in boron nitride", Phys. Rev. B 55 (1997) pp. 12025-12037

28 I. Jimenez, A. Jankowski, L. J. Terminello, J. A. Carlisle, D. G. Sutherland, G. L. Doll, J. V. Mantese, W. M. Tong, D. K. Shuh and F. J. Himpsel, "Near-edge x-ray absorption fine structure study of bonding modifications in BN thin films by ion implantation", Appl. Phys. Lett. 68 (1996) pp. 2816-2818

29 T. Sato, T. Ishii and N. Setaka, "Formation of cubic boron nitride from rhombohedral boron nitride by explosive shock compression", J. Am. Cer. Soc. 65 (1982) C-162

30 M. Ueno, K. Hasegawa, R. Oshima, A. Onodera, O. Shimomura, K. Takemura, H. Nakae, T.

Matsuda and T. Hirai, "Room-temperature transition of rhombohedral-type boron nitride under high static pressure", Phys. Rev. B 45 (1992) pp. 10226-10230

31 O. Mishima, S. Yamaoka and O. Fukunaga, "Crystal growth of cubic boron nitride by temperature difference method at ~55 kbar and ~1800°C", J. Appl. Phys. 61 (1987) pp. 2822-2825

32 C. Weissmantel, K. Bewilogua, D. Dietrich, H.-J. Erler, H.-J. Hinneberg, S. Klose, W. Nowick and G. Reisse, "Structure and properties of quasi-amorphous films prepared by ion beam techniques", Thin Solid Films 72 (1980) pp. 19-31

33 C. Weissmantel, "Ion beam deposition of special film structures", J. Vac. Sci. Technol. 18 (1981) pp. 179-185

34 S. Shanfield and R. Wolfson, "Ion beam synthesis of cubic boron nitride", J. Vac. Sci. Technol. A 1 (1983) pp. 323-325

35 W. Halverson and D. T. Quinto, "Effects of charge neutralization on ion-beam-deposited boron nitride films", J. Vac. Sci. Technol. A 3 (1985) pp. 2141-2146

36 H. Hofsaess, C. Ronning, U. Griesmeier, M. Gross, S. Reinke and M. Kuhr, "Cubic boron nitride films grown by low energy B^+ and N^+ ion beam deposition", Appl. Phys. Lett. 67 (1995) pp. 46-48

37 D. J. Kester and R. Messier, "Phase control of cubic boron nitride thin films", J. Appl. Phys. 72 (1992) pp. 504-513

38 T. A. Friedmann, P. B. Mirkarimi, D. L. Medlin, K. F. McCarty, E. J. Klaus, D. R. Boehme, H. A. Johnsen, M. J. Mills, D. K. Ottesen and J. C. Barbour, "Ion-assisted pulsed laser deposition of cubic boron nitride films", J. Appl. Phys. 76 (1994) pp. 3088-3101

39 M. Mieno and T, Yoshida, "Preparation of cubic boron nitride films by radio frequency bias sputtering", Surf. Coat. Technol. 52 (1992) pp. 87-92

40 M. Mieno and T. Yoshida, "Preparation of cubic boron nitride films by rf sputtering", Jpn. J. Appl. Phys. 29 (1990) pp. L1175-L1177

41 D. R. McKenzie, W. D. McFall, W. G. Sainty, C. A. Davis and R. E. Collins, "Compressive stress induced formation of cubic boron nitride", Diamond and Related Materials 2 (1993) pp. 970-976.

42 D. R. McKenzie, W. D. McFall, H. Smith, B. Higgins, R. W. Boswell, A. Durandet, B. W. James and I. S. Falconer, "High pressure phases produced by low energy ion implantation with reference to cubic boron nitride", Nucl. Instr. Meth. in Phys. Res. B 106 (1995) pp. 90-95

43 S. Kidner, C. A. Taylor II and R. Clarke, "Low energy kinetic threshold in the growth of cubic boron nitride films", Appl. Phys. Lett. 64 (1994) pp. 1859-1861

44 T. Ichiki and T. Yoshida, "Preparation of cubic boron nitride films by low pressure inductively coupled plasma enhanced chemical vapor deposition", Appl. Phys. Lett. 64 (1994) pp. 851-853

45 L. B. Hackenberger, L. J. Pilione, R. Messier and G. P. Lamaze, "Effect of stoichiometry on the phases present in boron nitride films", J. Vac. Sci. Technol. A 12 (1994) pp. 1569-

1575

46 D. J. Kester, K. S.Ailey, D. J.Lichtenwalner and R. F. Davis, "Growth and characterization of cubic boron nitride thin films", J. Vac. Sci. & Technol. A 12 (1994) pp. 3074-3081

47H. Hofsaess, H. Feldermann, M. Sebastian and C. Ronning, "Thresholds for the phase formation of cubic boron nitride thin films", Phys. Rev. B 55 (1997) pp. 13230-13233

48 P. B. Mirkarimi, K. F. McCarty, D. L. Medlin, W. G. Wolfer, T. A. Friedmann, E. J. Klaus, G. F. Cardinale and D. G. Howitt, "On the role of ions in the formations of cubic boron nitride films by ion-assisted deposition", J. Mater. Res. 9 (1994) pp. 2925-2938

49J. A. Thornton, J. Tabock and D. W. Hoffman, "Internal stresses in metallic films deposited by cylindrical magnetron sputtering", Thin Solid Films 64 (1979) pp. 111-119

50H. Windischmann, "An intrinsic stress scaling law for polycrystalline thin films prepared by ion beam sputtering", J. Appl. Phys. 62 (1987) pp. 1800-1807

51 S. Ulrich, J. Scherer, J. Schwan, I. Barzen, K. Jung and H. Ehrhardt, "Radio frequency ion plating-induced phase transition from h-BN to nanocrystalline c-BN", Diamond and Related Materials 4 (1995) pp. 288-291

52 Y. Lifshitz, S. R. Kasi, J. W. Rabalais and W. Eckstein, "Subplantation model for film growth from hyperthermal species", Phys. Rev. B 41 (1990) pp. 10468-10480

53 Y. Lifshitz, S. R. Kasi and J. W. Rabalais, "Subplantation model for film growth from hyperthermal species: Application to diamond", Phys. Rev. Lett. 62 (1989) pp. 1290-1293

54J. Robertson, "Deposition mechanisms for promoting sp^3 bonding in diamond-like carbon", Diamond and Related Materials 2 (1993) pp. 984-989

55 J. Robertson, "Deposition mechanism of cubic boron nitride", Diamond and Related Materials 5 (1996) pp. 519-524

56 D. J. Kester, K. S. Ailey, R. F. Davis and K. L. More, "Phase evolution in boron nitride thin films", J. Mater. Res. 8 (1993) pp. 1213-1216.

57 D. L. Medlin, T. A. Friedmann, P. B. Mirkarimi, P. Rez, M. J. Mills and K. F. McCarty, "Microstructure of cubic boron nitride thin films grown by ion-assisted pulsed laser deposition", J. Appl. Phys.76 (1994) pp. 295-303

58 H. Luethje, K. Bewilogua, S. Daaud, M. Johansson and L. Hultman, "Preparation of cubic boron nitride films by use of electrically conductive boron carbide targets", Thin Solid Films 257 (1995) pp. 40-45

59 S. Watanabe, S. Miyake, W. Zhou, Y. Ikuhara, T. Suzuki and M. Murakawa, "Transmission electron microscopic study of c-BN films deposited on a Si substrate", Appl. Phys. Lett., 66 (1995) pp. 1478-1480

60 H. Hofsaess, C. Ronning, U. Griesmeier, M. Gross, S. Reinke, M. Kuhr, J. Zweck and R. Fischer, "Characterization of cubic boron nitride films grown by mass separated ion beam deposition". Nucl. Instr. Meth. in Phys. Res. B 106 (1995) pp. 153-158

61 H. Yamashita, K. Kuroda, H. Saka, N. Yamashita, T. Watanabe and T. Wada, "Cross-

sectional transmission electron microscopy observations of c-BN films deposited on Si by ion-beam-assisted deposition", Thin Solid Films 253 (1994) pp. 72-77

62 T. Matsuda, N. Uno, H. Nakae and T. Hirai, "Synthesis and structure of chemically vapour-deposited boron nitride", J. Mater. Sci. 21 (1986) pp. 649-658.

63 E. G. Gerstner, D. R. McKenzie, M. K. Puchert, P. Y. Timbrell and J Zou, "Adherent carbon film deposition by cathodic arc with implantation", J Vac. Sci. Technol. A 13 (1995) pp. 406-411

64 O. Tsuda, Jun-ichi Fujikata, Y. Yamada and T. Yoshida, "Preparation of cubic boron nitride films by phase regulated rf bias sputtering", Advances in New Diamond Science and Technology, edited by S. Saito et al., MYU, Tokyo (1994) pp. 595-598

65 O. Tsuda, Y. Yamada, Y. Tatebayashi and T. Yoshida, "Effects of phase regulation on ion energy distribution in RF bias sputtering", proceedings for ACPST '96

66 Powder diffraction file, published by the Joint Committee on Powder Diffraction Standards p.491, 696, 790

67 T. L. Barr and S. Seal, "Nature of the use of adventitious carbon as a binding energy standard", J. Vac. Sci. Technol. A 13 (1995) pp. 1239-1246

68 T. Ichiki, S. Amagi and T. Yoshida, "Initial stage of cubic boron nitride film growth from vapor phase", J. Appl. Phys., 79 (1996) pp 4381-4387

69 K.-L. Barth, W. Sigle, D. Stoeckle, J. Ulmer and A. Lunk, "Deposition of cubic boron nitride layers - characterization of substrate-layer interface", Thin Solid Films 301 (1997) pp. 65-70

70 S. Ilias, V. Stambouli, J. Pascallon, D. Bouchier and G. Nouet, "Microstructure and stress investigations of cubic boron nitride thin films", submitted to the proceedings of Diamond '97

71 S. Tanuma, C. J. Powell and D. R. Penn, "Calculations of electron inelastic mean free paths (IMFPs) IV. Evaluation of calculated IMFPs and of the predictive IMFP formula TPP-2 for electron energies between 50 and 2000 eV", Surface Interface Anal. 20 (1993) pp. 77-89

72 A. Iwamoto and T. Yoshinobu, "Self-affine growth of copper electrodeposits", Phys. Rev. B 48 (1993) pp. 8282-8285.

73 K. L. Westra and D. J. Thomson, "Effect of tip shape on surface roughness measurements from atomic force microscopy images of thin films", J. Vac. Sci. & Technol., B 13 (1995) pp. 344-349

74 A. Iwamoto, T. Yoshinobu and H. Iwasaki, "Stable growth and kinetic roughening in electrochemical deposition", Phys. Rev. Lett. 72 (1994) pp. 4025-4028.

75 J. Krim, I. Heyvaert, C. Van Haesendonck and Y. Bruynseraede, "Scanning tunneling microscopy observation of self-affine fractal roughness in ion-bombarded film surfaces", Phys. Rev. Lett., 70 (1993) pp. 57-60.

76 A. -L. Barabasi and H. E. Stanley, Fractal concepts in surface growth, Cambridge University Press, Cambridge, First edn. (1995) p.20-37.

77 Y. -L. He, H. -N. Yang, T. -M. Lu and G. -C. Wang, "Measurements of dynamic scaling from epitaxial growth front : Fe film on Fe(001)", Phys. Rev. Lett., 69 (1992) pp. 3770-3773.

78 T. Yoshinobu, A. Iwamoto and H. Iwasaki, "Mesoscopic roughness characterization of grown surfaces by atomic force microscopy", Jpn. J. Appl. Phys., 33 (1994) pp. L67-L69.

79 O. Vatel, E. Andre, F. Chollet, P. Dumas and F. Salvan, "Atomic force microscopy studies of polysilicon growth during deposition on silicon", J. Vac. Sci. & Technol. B12 (1994) pp. 2037-2039

80 M. Z. Karim, D. C. Cameron and M. S. J. Hashmi, "Vapour deposited boron nitride thin films", Materials & Design 13 (1992) pp. 207-214

81 S. P. S. Arya and A. D'Amico, "Preparation, properties and applications of boron nitride thin films", Thin Solid Films 157 (1988) pp. 267-282

82H. Saitoh and W. A. Yarbrough, "Growth of cubic boron nitride from vapor phase", Diamond and Related Materials 1 (1992) pp. 137-146

83T. Yoshida, "Vapour phase deposition of cubic boron nitride",Diamond and Related Materials 5 (1996) pp. 501-507

84T. Yoshida, "State-of-the-art vapor-phase deposition of cubic boron nitride", Diamond Films and Technology 7 (1997) pp. 87-104

85 F. Richter, "Cubic boron nitride and carbon nitride films: Recent developments", Diamond Materials IV (Electrochemical Society Proceedings Volume 95-4 (1995) pp.347-358

86 K. Bewilogua, "Preparation and characterization of cubic boron nitrde and carbon nitride films", Science 280 (1996) pp. 213-218

87 H. Hofsaess and C. Ronning, "Ion beam deposition and doping of diamondlike materials", ASM Conference Proceedings of the International Conference on "Beam Processing of Advanced Materials" (1996) pp. 29-56

88 P. B. Mirkarimi, K. F. McCarty and D. L. Medlin, "Review of advances in cubic boron nitride film synthesis", to appear in Materials Science and Engineering Reports

89 L. B. Hackenberger, L. J. Pilione and R. Messier, "Bombardment stabilization of cubic boron nitride", Science and Technology of Thin Films edited by F. C. Matacotta and G. Ottaviani (1995) pp. 121-144

90 M. E. O'Hern and C. J. McHargue, "Mechanical properties testing of diamond and diamond-like films by ultra-low load indentation", Diamond and Diamond-Like Films and Coatings, edited by R. E. Clausing et al., Plenum Press, NY (1991) pp. 715-721

91 M. E. O'Hern, C. J. McHargue, R. E. Clausing, W. C. Oliver and R. H. Parrish, "Determination of the mechanical properties of diamond and diamond-like films by the ultra-low load indentation technique", 1989 Materials Research Society, Extended abstract, pp. 131-137

92K. Inagawa, K. Watanabe, H. Ohsone, K. Saitoh and A. Itoh, "Preparation of cubic boron

nitride film by activated reactive evaporation with a gas activation nozzle", J. Vac. Sci. Technol. A5 (1987) pp. 2696-2700

93 M. Murakawa and S. Watanabe, "The synthesis of cubic BN films using a hot cathode plasma discharge in a parallel magnetic field", Surf. Coat. Technol. 43/44 (1990) pp. 128-136

94 D. R. McKenzie, "Generation and applications of compressive stress induced by low energy ion beam bombardment", J. Vac. Sci. Technol. B 11 (1993) pp. 1928-1935

95 P. B. Mirkarimi, D. L. Medlin, K. F. McCarty, D. C. Dibble, W. M. Clift, J. A. Knapp and J. C. Barbour, "The synthesis, characterization, and mechanical properties of thick, ultrahard cubic boron nitride films deposited by ion-assisted sputtering", J. Appl. Phys. 82 (1997) pp. 1617-1625

96 W. C. Oliver and G. M. Pharr, "An improved technique for determining hardness and elastic modulus using load and displacement sensing indentation experiments", J. Mater. Res., 7 (1992) pp. 1564-1583

97 K. L. Johnson, Contact mechanics, Cambridge University Press, First paperback edn., (1987) p. 93

98 G. M. Pharr, D. L. Callahan, S. D. McAdams, T. Y. Tsui, S. Anders, A. Anders, J. W. Ager III, I. G. Brown, C. S. Bhatia, S. R. P. Silva and J. Robertson, "Hardness, elastic modulus, and structure of very hard carbon films produced by cathodic-arc deposition with substrate pulse biasing", Appl. Phys. Lett. 68 (1996) pp. 779-781

99 G. G. Stoney, "The tension of metallic films deposited by electrolysis", Proc. R. Soc. London Ser. A 82 (1909) pp. 172-175

100 D. E. Fahnline, C. B. Masters and N. J. Salamon, "Thin film stress from nonspherical substrate bending measurements", J. Vac. Sci. & Technol. A 9 (1991) pp. 2483-2487

101 W. A. Brantley, "Calculated elastic constants for stress problems associated with semiconductor devicees", J. Appl. Phys. 44 (1973) pp. 534-535

102 M. Friedrich, J. Hahn, S. Laufer, F Richter, H.-J. Hinneberg, and D. R. T. Zahn, "The formation of cubic boron nitride and silicon carbide layers on silicon", Diamond Materials IV, edited by K. V. Ravi and J. P. Dismukes, The Electrochemical Society (1995) pp. 394-402

103 G. F. Cardinale, D. G. Howitt, K. F. McCarty, D. L. Medlin, P. B. Mirkarimi and N. R. Moody, "Analysis of residual stress in cubic boron nitride thin films using micromachined cantilever beams", Diamond and Related Materials 5 (1996) pp. 1295-1302

104 Z. Li, L. Wang, T. Suzuki, A. Argoitia, P. Pirouz and J. C. Angus, "Orientation relationship between chemical vapor deposited diamond and graphite substrates", J. Appl. Phys. 73 (1993) pp. 711-715

105 D. L. Medlin, T. A. Friedman, P. B. Mirkarimi, G. F. Cardinale and K. F. McCarty, "Crystallographic texture in cubic boron nitride thin films", J. Appl. Phys. 79 (1996) pp. 3567-3571

106 S. Reinke, M. Kuhr and W. Kulisch, "Investigation of stress and adhesion of cubic boron nitride films", Diamond and Related Materials 5 (1996) pp. 508-513

107 Y. Matsui, Y. Sekikawa, T. Sato and T. Ishii, "Formations of rhombohedral boron nitride, as revealed by TEM-electron energy loss spectroscopy", J. Mater. Sci. 16 (1981) pp. 1114-1116

108 D. L. Medlin, T. A. Friedman, P. B. Mirkarimi, M. J. Mills and K. F. McCarty, "Evidence for rhombohedral boron nitride in cubic boron nitride films grown by ion-assisted deposition", Phys. Rev. B 50 (1994) pp. 7884-7887

109 R. M. Wentzcovitch, S. Fahy, M. L. Cohen and S. G. Louie, "Ab initio study of graphite → diamondlike transitions in BN", Phys. Rev. B 38 (1988) pp. 6191-6195

110. W. R. Lambrecht, C. H. Lee, B. Segal, J. C. Angus, Z. Li and M. Sunkara, "Diamond nucleation by hydrogenation of the edges of graphitic precursors", Nature 364 (1993) pp. 607-610

111. W. T. Zheng, H. Sjoestroem, I. Ivanov, K. Z. Xing, E. Broitman, W. R. Salaneck, J. E. Greene and J.-E. Sundgren, "Reactive magnetron sputter deposited CNx: Effects of N2 pressure and growth temperature on film composition, bonding, and microstructure", J. Vac. Sci. Technol. A 14 (1996) pp. 2696-2701

112. D. G. McCulloch, N. A. Marks, D. R. McKenzie and S. Prawer, "Molecular dynamics and experimental studies of preferred orientation induced by compressive stress", Nucl. Instr. Meth. Phys. Res. B 106 (1995) pp.545-549

113. R. W. Lynch and H. G. Drickamer, "Effect of high pressure on the lattice parameters of diamond, graphite and hexagonal boron nitride", J. Chem. Phys. 44 (1966) pp. 181-184

114. M. Roeder, J. Hahn, U. Falke, S. Schulze, F. Richter and M. Hietschold, " Electron microscopic phase analysis of BN-thin films", Mikrochim. Acta 125 (1997) pp. 283-286

115. G. F. Cardinale, D. L. Medlin, P. B. Mirkarimi, K. F. McCarty and D. G. Howitt, "Orientation-dependence of elastic strain energy in hexagonal and cubic boron nitride layers in energetically deposited BN films", J. Vac. Sci. Technol. A 15 (1997) pp. 196-200

116. S. Horiuchi, L.-L. He, M. Onoda and M. Akaishi, "Monoclinic phase of boron nitride appearing during the hexagonal cubic phase transition at high pressure and high temperature", Appl. Phys. Lett. 68 (1996) pp 182-184

117. N. Bozzolo, E. Bauer-Grosse, S. Ilias, V. Stambouli, J. Pascallon, D. Bouchier and J. Ghanbaja, "Texture investigations by a TEM of IBAD deposited c-BN films", submitted to Appl. Phys. Lett.

118. P. B. Mirkarimi, D. L. Medlin, K. F. McCarty and J. C. Barbour, "Growth of cubic BN films on β-SiC by ion-assisted pulsed laser deposition", Appl. Phys. Lett. 66 (1995) pp. 2813-2815

119. W.-L. Zhou, Y. Ikuhara and T. Suzuki, "Orientational relationship between cubic boron nitride and hexagonal boron nitride in a thin film synthesized by ion plating", Appl. Phys. Lett. 67 (1995) pp. 3551-3553

120. W.-L. Zhou, Y. Ikuhara, M. Murakawa, S. Watanabe and T. Suzuki, "Direct observation of hexagonal boron nitride at the grain boundary of cubic boron nitride by high resolution

electron microscopy", Appl. Phys. Lett. 66 (1995) pp. 2490-2492

121 Z. -M. Yu, T. Rogelet and S. A. Flodstroem, "Diamond growth on turbostratic carbon by hot filament chemical vapor deposition", J. Appl. Phys. 74 (1993) pp. 7235-7240

122. A. K. Ballal, L. Salamanca-Riba, G. L. Doll, C. A. Taylor II and R. Clarke, "Ion-assisted pulsed laser deposition of cubic BN films on Si (001) substrates", J. Mater. Res. 7 (1992) pp. 1618-1620

123. A. K. Ballal, L. Salamanca-Riba, C. A. Taylor II and G. L. Doll, "Structural characterization of preferentially oriented cubic BN films grown on Si(001) substrates", Thin Solid Films 224 (1993) pp. 46-51

124 W. Dworschak, K. Jung and H. Ehrhardt, "Growth mechanism of cubic boron nitride in a r. f. glow discharge", Thin Solid Films 254 (1995) pp. 65-74

125. K. S. Park, D. Y. Lee, K. J. Kim and D. W. Moon, "Observation of a hexagonal BN surface layer on the cubic BN film grown by dual ion beam sputter deposition", Appl. Phys. Lett. 70 (1997) pp. 315-317

126. G. Sene, D. Bouchier, S. Ilias, M. A. Djouadi, J. Pascallon, V. Stambouli, P. Moeller and G. Hug, "Correlation between microstructure and collisional effects in cubic boron nitride synthesized using IBAD", Diamond and Related Materials 5 (1996) pp. 530-534

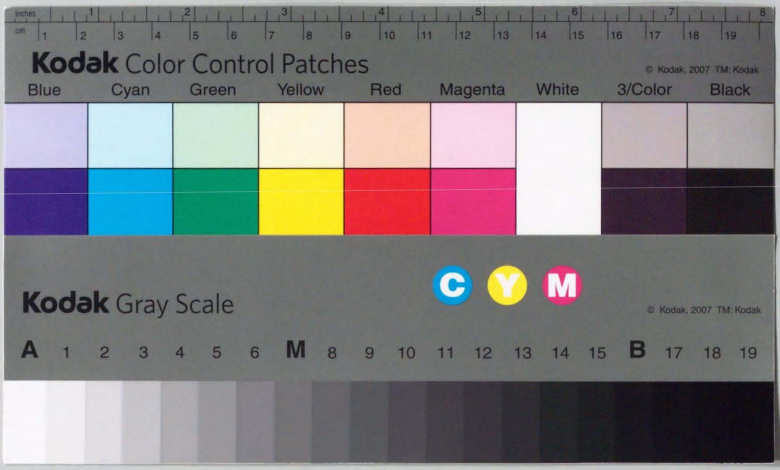
inches
cm
Kodak Color Control Patches
© Kodak, 2007 TM: Kodak
Blue
Cyan
Green
Yellow
Red
Magenta
White
3/Color
Black
Kodak Gray Scale
C
Y
M
© Kodak, 2007 TM: Kodak
A 1 2 3 4 5 6 M 8 9 10 11 12 13 14 15 B 17 18 19